Title

Tuning Bulk Redox and Altering Interfacial Reactivity in Highly Fluorinated Cation-Disordered Rocksalt Cathodes

Journal

ACS Applied Materials & Interfaces, 15(15)

ISSN

1944-8244

Authors

Crafton, Matthew J

Huang, Tzu-Yang

Yue, Yuan

et al.

Publication Date

2023-04-19

DOI

10.1021/acsami.2c16974

Tuning Bulk Redox and Altering Interfacial Reactivity in Highly Fluorinated Cation-Disordered Rocksalt Cathodes

Matthew J. Crafton, Tzu-Yang Huang, Yuan Yue, Raynald Giovine, Vincent Wu, Chaochao Dun, Jeffrey J. Urban, Raphaële J. Clément, Wei Tong, Bryan D. McCloskey

June 2022

1 Abstract

Lithium-excess, cation-disordered rocksalt (DRX) materials have been subject to intense scrutiny and development in recent years as potential cathode materials for Li-ion batteries. Despite their compositional flexibility and high initial capacity, they suffer from poorly understood parasitic degradation reactions at the cathode-electrolyte interface. These interfacial degradation reactions deteriorate both the DRX material and electrolyte, ultimately leading to capacity fade and voltage hysteresis during cycling. In this work, differential electrochemical mass spectrometry (DEMS) and titration mass spectrometry are combined to quantify the extent of bulk redox and surface degradation reactions for a set of $Mn^{2+/4+}$-based DRX oxyfluorides during initial cycling with a high voltage charging cutoff (4.8 V vs. Li/Li^+). Increasing the fluorine content from 7.5% to 33.75% is shown to deactivate oxygen redox and suppresses high-voltage O_2 evolution from the DRX surface. Additionally, electrolyte degradation resulting in the formation of both gaseous species and soluble protic species is observed. Subsequently, DEMS is paired with a fluoride-scavenging additive to demonstrate that increasing fluorine content leads to increased dissolution of fluorine from the DRX material into the electrolyte. Finally, a suite of *ex-situ* spectroscopy techniques (X-Ray photoelectron spectroscopy, inductively coupled plasma optical emission spectroscopy, and solid-state nuclear magnetic resonance spectroscopy) are employed to study the change in DRX composition during charging, revealing the dissolution of manganese and fluorine from the DRX material at high voltages. This work provides insight into the degradation processes occurring at the DRX-electrolyte interface and points towards potential routes of mitigating the deleterious processes.

2 Introduction

The electric vehicle and portable electronic industries have created an enormous demand for low cost, high energy density, resource friendly lithium ion (Li-ion) batteries. The ability of the current commercial battery technology to meet this demand is limited in large part by the cathode active material, which commonly consists of a layered lithium transition metal oxide (TMO) such as $LiCoO_2$ or $Li(Ni_xMn_yCo_z)O_2$ [1, 2]. These materials possess a limiting electrochemical capacity compared to most prospective anode materials (graphite, Li, etc), thereby limiting the energy density of the full electrochemical cell [3, 4]. Furthermore, TMO's often contain scarce or expensive transition metals like Co, raising the cost and limiting the supply of TMO-based cathode materials [5, 6]. This limitation has spurred an enormous effort to develop alternative cathode materials with low cost, resource friendly compositions and high electrochemical capacities [7, 8, 9]. From these efforts, lithium-excess cation-disordered rocksalt (DRX) materials have emerged as a promising class of transition metal oxides and oxyfluorides that display several characteristics that are desirable for applications as Li-ion cathode materials [10].

DRX materials exhibit the $\alpha - LiFeO_2$ structure wherein the cations (Li, transition metals) and anions (oxygen, fluorine) possess no long-range order throughout the material, although numerous studies have demonstrated the presence and role of short-range order in DRX materials [11, 12, 13, 14]. This feature is

contrasted to the $\alpha - NaFeO_2$ structure of layered TMO cathode materials, in which the cations are arranged in alternating layers of lithium and transition metals [2].

The cation-disordered structure of DRX materials confers a degree of compositional flexibility that allows for the incorporation of transition metals and anions that are incompatible with layered TMO's, which must maintain their layered structure during cycling. For example, $Ni^{2+/4+}$ and $Co^{3+/4+}$ are the predominantly available transition metal redox couples in layered TMO's because their electronic structure prevents site migration during cycling, a process that would otherwise disrupt the layered structure and impede Li transport [11, 15]. Although Mn is often included in layered TMO's, it must remain electrochemically inactive in the Mn^{4+} state to prevent migration into the Li layer [16]. However, because the requirement to form and maintain a layered structure is removed in the case of DRX materials, a wide range of transition metals like Mn, Ni, Fe, V, Cr, and Mo can be employed to provide charge compensation [17, 18, 19]. The expanded range of accessible transition metals allows for the incorporation of low-cost, Co-free redox centers like Mn and Fe. The compositional flexibility conferred by the cation-disordered structure also allows for the incorporation of fluorine into the anion lattice of DRX materials [20]. In contrast, achieving fluorine incorporation into the anion lattice of layered TMO's is infeasible, and attempts have led instead to the formation of a LiF surface coating [21]. Fluorine substitution has previously been shown to improve the high-voltage stability of DRX cathode materials by suppressing surface degradation processes like oxygen loss and mitigating the extent of structural transformation to a spinel-like phase [22, 23, 24]. Furthermore, by lowering the average anion valence, fluorination enables the inclusion of transition metals in the 2+ oxidation state, allowing for the utilization of two-electron redox couples like $Mn^{2+/4+}$. Such 'double' redox couples are desirable because they can provide twice as much charge compensation per transition metal as a one-electron redox couple. Therefore, the compositional flexibility conferred by the cation-disordered structure greatly enhances the variety and tunability of DRX materials, allowing the formulation of DRX materials with resource friendly composition and high stability [25, 26, 24].

The cation-disordered structure of DRX materials also creates a large amount of local environments referred to as Li-O-Li configurations, in which two Li ions are bonded to an oxygen atom on opposite sides from one another. Li-O-Li configurations, which do not exist in perfectly ordered layered TMO's without Li-excess composition, give rise to an electronic structure in which bulk oxygen redox may occur at potentials in the range of 4.0-4.6 V vs. Li/Li^+ [27]. The abundance of Li-O-Li configurations induced by the cation-disordered structure therefore creates another potentially reversible redox reservoir in DRX materials, increasing the capacity available during cycling. These two features of compositional flexibility and abundance of Li-O-Li configurations, both of which are consequences of the cation-disordered structure, make DRX materials promising candidates for next-generation cathode materials.

Despite these promising characteristics, DRX materials still suffer from several issues that limit their long-term cyclability. One key limitation is the degradation imposed by the high interfacial reactivity of DRX cathode materials. Extracting the promisingly high capacities from DRX materials requires cycling to high potentials (4.8 V vs. Li/Li^+), which leads to degradation at the cathode-electrolyte interface. This degradation drives the depletion of electrolyte; formation of a densified, reduced TMO layer; generation of reactive electrolyte degradation products; and evolution of gaseous species such as O_2 and CO_2 [22, 23, 28]. In turn, these processes lead to capacity loss and impedance rise in the cell, limiting the attainable energy density from cells containing DRX materials [18, 24].

To address these shortcomings, there have been many efforts to improve the stability and cyclability of DRX materials [19, 22, 23, 29]. In this work, we leverage the compositional flexibility of DRX materials by studying a set of DRX oxyfluorides with varying degrees of fluorination and, hence, $Mn^{2+/4+}$ redox. The DRX materials investigated are LMNOF-4515 ($Li_{1.2}Mn_{0.45}Nb_{0.35}O_{1.85}F_{0.15}$), LMNOF-6060 ($Li_{1.2}Mn_{0.60}Nb_{0.20}O_{1.40}F_{0.60}$), and LMNOF-6368 ($Li_{1.2}Mn_{0.625}Nb_{0.175}O_{1.325}F_{0.675}$). The bulk redox processes and electrochemical performance of these materials during extended cycling has been studied in a previous publication by Yue et al. [18]. These materials achieve bulk charge compensation during cycling via two primary electrochemical processes: $Mn^{2+/4+}$ redox and oxygen redox. They also contain electrochemically-inactive Nb^{5+}, which stabilizes the disordered structure. Herein, we conduct *ex-situ* acid titration mass spectrometry (TiMS) on cycled cathodes to demonstrate that increasing fluorination from 7.5% to 33.75% deactivates bulk oxygen redox in DRX materials, shifting the entirety of the electrochemical capacity to $Mn^{2+/4+}$ redox. We also couple TiMS with *in-situ* differential electrochemical mass spectrometry (DEMS) to show that increasing the fluorine content in DRX materials influences the surface reactivity of

DRX cathodes, stabilizing surface carbonate species at high voltages. We then extend our DEMS analysis over multiple cycles, demonstrating that fluorination suppresses high-voltage oxygen evolution from DRX cathodes and revealing multiple modes of electrolyte degradation that slowly diminish throughout cycling for all three DRX materials. Next, we introduce into our DEMS cells a fluoride-scavenging electrolyte additive to observe fluorine dissolution from the DRX materials *in-situ*, showing that increasing DRX fluorine content increases the amount of fluorine that dissolves from the DRX material into the electrolyte [30, 31]. Finally, we use X-Ray photoelectron spectroscopy (XPS), inductively coupled plasma optical emission spectroscopy (ICP-OES), and solid-state nuclear magnetic resonance spectroscopy (SS-NMR) to monitor the change in DRX composition during the first charge, revealing the deposition of electrolyte degradation products and the dissolution of DRX-originating Mn and F.

3 Methods

Synthesis of Li-excess $LiMn^{2+}Nb^{5+}OF$ DRX Materials. All $LiMn^{2+}Nb^{5+}OF$ DRX materials were synthesized via a mechanochemical reaction. Precursors of lithium oxide, manganese (II) oxide, niobium (V) oxide, and lithium fluoride were used. All precursors were weighed stoichiometrically except lithium oxide (10% excess) and loaded inside a stainless-steel jar, then sealed tightly inside an Ar-fill glove box. The precursors were high-energy milled extensively until the pure rocksalt phase was formed. The milled powder was then collected inside the glove box. Detailed synthesis conditions can be found in our previous report [18].

Cathode Preparation. The as-synthesized DRX active material was first mixed with acetylene black (AB) conductive carbon powder in a DRX:AB ratio of 6:3 (wt:wt). Cathodes for all experiments besides fluoride-scavenging DEMS were made using a slurry mixing technique. The DRX-AB powder mixture was mixed with a solution of 10wt% polyvinylidene fluoride (PVDF) binder dissolved in N-Methyl-2-pyrrolidone (NMP) in a mortar and pestle until a uniform slurry was formed. The DRX:AB powder and PVDF/NMP solution were combined to produce an approximate composition of 60:30:10 (wt) DRX:AB:PVDF. The resulting slurry was then spread onto stainless steel mesh and dried at 80°C for 30 minutes. After this brief initial drying, the electrodes were pressed with uniform pressure using a screw-driven clamp and dried overnight under vacuum at 120°C. For fluoride-scavenging experiments, the electrodes were fabricated using a dry technique using polyethylene (PE) (Sigma) as the binder instead of PVDF. The DRX:AB mixture was combined with PE powder to produce an approximate composition of 60:30:10 (wt) DRX:AB:PE. The powders were ground together in a mortar and pestle, and the resulting mixture was placed on stainless steel mesh before being pressed into place using a steel pin. Typical DRX loading in all measurements was 7 mg cm^{-}2, and all electrodes were 1/2 inch in diameter (1.3 cm^2).

Electrochemical Cell Preparation. Custom-built Swagelok cells were used as described previously [32, 33, 34]. Li foil was used as the counter electrode in all cells except for those used to prepare electrodes for XPS analysis or those used to verify the H_2 formation mechanism. For the cells used to prepare electrodes for XPS analysis, the counter electrode was graphite. For the control experiments verifying the formation mechanism of H_2, the counter electrode was delithiated lithium iron phosphate. The separator in all cells was composed of 1 sheet of Whatman QMA filter paper (on the counter electrode side) and 1 sheet of Celgard 2500 (on the DRX side). The electrolyte varied depending on the type of experiment. For DEMS experiments measuring the evolution of O_2, CO_2, and H_2, the electrolyte was 1M lithium hexafluorophosphate ($LiPF_6$) in 1:1 vol:vol mixture of ethylene carbonate (EC) / diethyl carbonate (DEC) (Sigma). For the experiments preparing electrodes for XPS analysis, the electrolyte was also 1M $LiPF_6$ in 1:1 EC:DEC. For DEMS experiments monitoring fluoride dissolution from the DRX material, the electrolyte was 1M lithium bis(trifluoromethanesulfonyl)imide (LiTFSI, Sigma) in 1:1 vol:vol EC/DEC with 1vol% tris(trimethylsilyl)phosphate (TMSPa, Sigma). For all DEMS cells, the electrolyte loading was 60 μL/cm^2. Despite the low concentration of TMSPa in the electrolyte for fluoride-scavenging DEMS cells, the highest amount of fluoride formation observed in any experiment was a fraction of the amount of TMSPa present ($\sim$ 30%), leading us to conclude that there is an excess of TMSPa in the electrolyte relative to the amount of fluoride available for reaction.

Electrochemical testing and DEMS gas analysis. The custom-built DEMS instrument and its operation was described in previous publications [32, 33, 34]. Hermetically-sealed, custom-built Swagelok cells were assembled in an Argon atmosphere glovebox and appropriately attached to the DEMS apparatus to avoid

air exposure. The cells were cycled on a Bio-Logic VSP-series potentiostat under positive Ar pressure (approximately 1.2 bar). For all experiments, cells were cycled at a current of 0.1 Li hr^{-1} (27.3 mA g^{-1} for LMNOF-4515, 28.6 mA g^{-1} for LMNOF-6060, and 28.8 mA g^{-1} for LMNOF-6368) to cut-off potentials listed with each experiment. In some cases, the cells were then held at the relevant cut-off potential until the current decayed to 10% of its original value, or 0.01 Li hr^{-1}. Throughout the experiment, the cell headspace was purged with 500 μL of Ar by the DEMS instrument every 10 minutes and any accumulated gases were swept to the mass spectrometer chamber for analysis. The apparatus is calibrated for O_2, CO_2, H_2, and trimethylsilyl fluoride (Me_3SiF) in Ar, allowing for the determination of the partial pressures of each analyte. The amount of each gas evolved was then quantified using the known volume, temperature, and partial pressure of the gas sample through the ideal gas law.

TiMS Analysis of DRX Powders and Electrodes. The design and operation of the custom-built TiMS instrument is nearly identical to that of the DEMS instrument, as described in previous publications [28, 32, 33, 34]. For studies on the as-synthesized materials, pristine cathodes were placed in a custom-built, hermetically sealed titration vessel. For studies on charged cathodes, rinsed and dried cathodes extracted from electrochemical cells were instead placed in the titration vessel. This vessel was then appropriately connected to the TiMS apparatus to avoid air exposure. During the experiment, the cell headspace was purged with 2 mL of Ar by the TiMS instrument every 2 minutes and any accumulated gases were swept to the mass spectrometer chamber for analysis. After establishing baseline levels for gases of interest, 1 mL of N_2-sparged 10M H_2SO_4 was injected into the titration vessel through a septum-sealed injection port. The resulting acid-cathode mixture was mixed with a magnetic stir bar. The apparatus is calibrated for O_2 and CO_2 in Ar, allowing for the determination of the partial pressures of each analyte. Gas samples were taken until the reaction was completed, as determined by the return of any analyte signals to their baseline levels. The amount of each gas evolved was then quantified using the partial pressure, volume, and temperature of each gas sample. For all charged cathode samples, the charging procedure consisted of a constant current charge to the listed cut-off voltage at 0.1 Li hr^{-1} followed by a potentiostatic hold at the cut-off until the current decayed to 0.01 Li hr^{-1}. After the voltage hold, the cell was returned to the glovebox, minimizing air exposure. Once inside the glovebox, the cell was disassembled and the cathode was placed in a dry vial. The cathode was rinsed three times with 200 μL DEC and dried under vacuum at room temperature for several hours. The dried cathodes were then stored in a sealed vial in the glovebox until TiMS analysis.

ICP-OES Analysis of Mn Dissolution. Inductively coupled plasma optical emission spectroscopy (ICP-OES) measurements were performed using a Perkin Elmer 5300 DV optical emission inductively coupled plasma spectrometer with an auto sampler. For all samples and standards, a matrix solution consisting of 2wt% HNO_3 (70%, Sigma Aldrich) and 0.1wt% $H_2C_2O_4$ (oxalic acid dihydrate, Suprapur, Sigma Aldrich) in deionized water was used. A manganese standard solution for ICP (Sigma Aldrich) was diluted with matrix solution to four different concentrations to calibrate manganese between 0-1 mg L^{-1}, and all sample measurements fell within the calibrated range. Electrolyte and anode samples were obtained from DRX cells by recovering the electrolyte-soaked separator and Li metal anode from Swagelok-type cells. To allow for easier removal, the Li metal anode was backed by a sheet of stainless steel foil. Each DRX material was subjected to three different cycling procedures: rest on open-circuit (OCV), charge to 4.0 V, and charge to 4.8 V. The OCV procedure consisted of simply allowing the cell to rest on open-circuit for 24 hours. The charging procedures consisted of a constant current charge at 0.1 Li hr^{-1} to the listed cutoff voltage followed by a potentiostatic hold at the cutoff voltage until the current decayed to 0.01 Li hr^{-1}. After the potentiostatic hold, the cell was allowed to rest at open-circuit until the cell had been intact for 24 hours, ensuring similar electrode-electrolyte contact times for all three cycling procedures. After the end of a cycling procedure, the cell was returned to an Ar-filled glovebox where the separator and anode were each separately extracted and dried under vacuum overnight. After drying, the separator and anode were separately dissolved in 20 mL of matrix solution. The resulting solutions were stored for three days to allow for full dissolution of Mn ions, after which the solutions were filtered. The concentration of Mn ions in the resulting filtered solution was then analyzed by ICP-OES, and the DRX-normalized manganese dissolution for each cell was back-calculated from the electrode loading and the sum of the amounts of Mn detected in the separator and electrolyte samples.

XPS Analysis of DRX Electrodes. X-ray photoelectron spectroscopy (XPS, Thermo Fisher, USA) measurements were conducted to analyze the chemical states of each element. The photoelectron spectrometer system is configured with an Al Kα excitation source with spot size of 400 μm. Before collecting XPS

spectrum, ion flood source is adopted for charge neutralization. XPS data were analyzed using CasaXPS software. The binding energy scale of the XPS spectra was calibrated from the C1s C-C peak at 284.8 eV, and peaks were fit with a LF lineshape on top of a Shirley background. For the charged sample of each DRX material, the charging procedure consisted of a constant current charge at 0.1 Li hr^{-1} to 4.8 V followed by a potentiostatic hold at 4.8 V until the current decayed to 0.01 Li hr^{-1}. After charging, the cell was returned to the Ar-filled glovebox, where the cathode was extracted, rinsed with DEC, and dried under vacuum overnight.

SS-NMR Analysis of DRX Powders and Electrodes Solid-state NMR spectra were recorded at B_0=2.35 T (100 MHz for ^{1}H) using a wide bore Bruker BioSpin spectrometer equipped with a DMX 500 MHz console and a custom made 1.3 mm X-broadband magic angle spinning (MAS) probe (tuned to ^{7}Li: 38.9 MHz or ^{19}F: 94.1 MHz). To avoid air exposure, samples were packed in zirconia rotors in an Ar-filled glovebox and spun at ν_R= 60 kHz using dry nitrogen. ^{19}F and ^{7}Li NMR chemical shifts were externally referenced against pure lithium fluoride powder (LiF, $\delta_{iso}(^{19}F) = -204$ ppm and $\delta_{iso}(^7Li) = -1$ ppm). Both ^{7}Li and ^{19}F MAS NMR spectra were obtained using a rotor synchronized spin-echo sequence (90° - τ_R - 180° - τ_R) with 90° radiofrequency (RF) pulses of 0.45 μs and 0.34 μs, respectively. For both nuclei, a total of 7616 transients were averaged with a recycle delay of 50 ms. This short recycle delay was enough to reach fully relaxed ^{7}Li NMR spectra while in ^{19}F NMR, only signal around −190 ppm (from F in the LMNOF cathode) were fully relaxed. In addition, isotropic ^{7}Li and ^{19}F NMR spectra were recorded using the projected magic angle turning phase-adjusted sideband separation (pj-MATPASS) pulse sequence which effectively removes spinning sidebands due to MAS [35, 36]. Both experiments used the same 90° RF pulses as their corresponding spin echoes and data were averaged over 4000 scans with a recycle delay of 50 ms. Solid-state NMR data were processed using Bruker TopSpin 3.6.0 and spectra were fitted using DMfit software [37]. For the charged sample of each DRX material, the charging procedure consisted of a constant current charge at 0.1 Li hr^{-1} to 4.8 V followed by a potentiostatic hold at 4.8 V until the current decayed to 0.01 Li hr^{-1}. After charging, the cell was returned to the Ar-filled glovebox, where the cathode was extracted, rinsed with DEC, and dried under vacuum overnight. For both the pristine and charged samples, electrode material containing DRX material, acetylene black, and PVDF was scraped from the stainless steel mesh current collector and collected for analysis. For the active material sample, the carbon-coated DRX powder containing only DRX material and acetylene black was used.

4 Results and Discussion

4.1 Comparison of Voltage Profiles

To interpret the bulk electrochemical properties of the DRX materials, all three LMNOF materials were subjected electrochemical cycling consisting of charging to 4.8 V and discharging to 1.5 V at a constant rate of 0.1 Li hr^{-1}. The voltage profiles for the first charge and discharge for LMNOF-4515, LMNOF-6060, and LMNOF-6368 are shown in Figure 1a. The initial charge capacities of LMNOF-4515, LMNOF-6060, and LMNOF-6368 were 269 mAh g^{-1}, 246 mAh g^{-1}, and 260 mAh g^{-1}, respectively. The initial discharge capacities, in contrast, were similar: 218 mAh g^{-1} for LMNOF-4515, 216 mAh g^{-1} for LMNOF-6060, and 212 mAh g^{-1} for LMNOF-6368. While the voltage profiles for all three materials possess the same general shape, that of LMNOF-4515 has more strongly defined charge plateaus around 3.5 V and 4.4 V, whereas those of LMNOF-6060 and LMNOF-6368 are more consistently sloping throughout the voltage range. The shape of the voltage profiles can be evaluated more rigorously by viewing the same voltage profile information in dQ dV^{-1} vs. V format (where Q is capacity), as shown in Figure 1b. In this format, it is apparent that the dQ dV^{-1} profile for the first charge of LMNOF-4515 has pronounced peaks centered at 3.5 V and 4.4 V, while the dQ dV^{-1} profiles for the first charge of LMNOF-6060 and LMNOF-6368 tend to be flatter and broader. This difference indicates that two primary redox processes in LMNOF-4515 provide bulk charge compensation at relatively well defined voltages in LMNOF-4515, whereas the primary redox processes in LMNOF-6060 and LMNOF-6368 provide charge compensation across a wider range of voltages. The less defined nature of the redox processes occurring during charging of LMNOF-6060 and LMNOF-6368, compared to those of LMNOF-4515, suggest a broader distribution of Li site energies in the more highly fluorinated materials. Since the distribution of Li site energies has been previously linked to the degree of disorder in DRX materials, this result may indicate that the more highly fluorinated LMNOF-6060 and

LMNOF-6368 possess less short-range ordering than LMNOF-4515 [13].

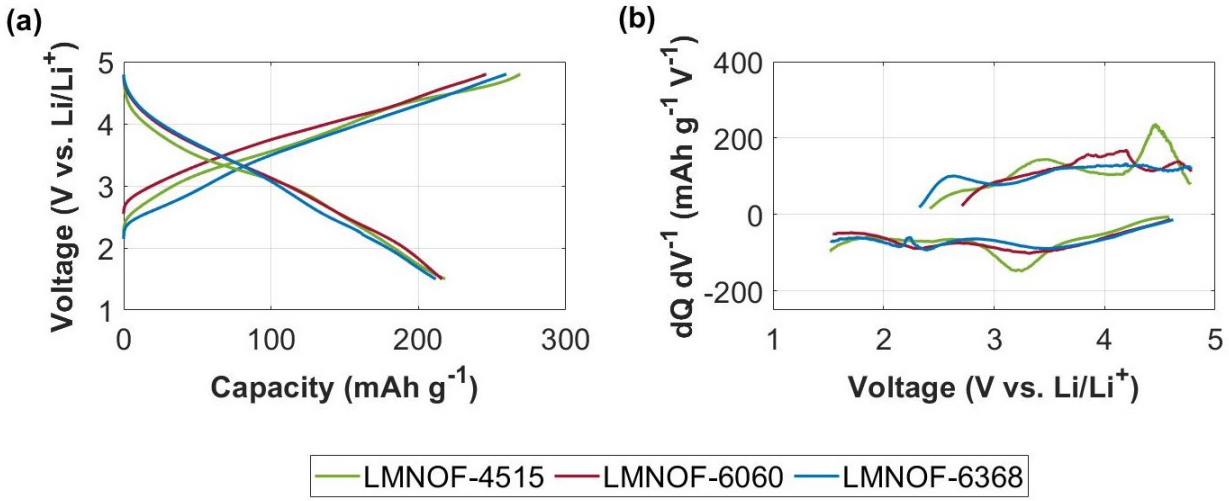

Figure 1: First charge-discharge comparison for the three LMNOF materials. (a) Voltage profiles during first charge-discharge and (b) corresponding $\mathrm{dQ\,dV^{-1}}$ for all three DRX materials. All materials were charged to 4.8 V vs. $\mathrm{Li/Li^+}$ and discharged to 1.5 V vs. $\mathrm{Li/Li^+}$ at a constant current rate of 0.1 Li $\mathrm{hr^{-1}}$.

Based on prior studies investigating the bulk redox processes occurring in LMNOF DRX materials, we ascribe the low-voltage (∼3.5 V) process in LMNOF-4515 to $\mathrm{Mn^{2+/4+}}$ redox and the high-voltage (∼4.4 V) process to oxygen redox [18]. In contrast, it is challenging to assign based on voltage profile information alone the electrochemical processes occurring in LMNOF-6060 and LMNOF-6368, as the voltage plateaus during cycling are less defined. To further understand and quantify the bulk redox processes supplying electrochemical capacity in these materials, quantitative *ex-situ* TiMS was employed to measure the amount of oxidized oxygen species in the DRX materials at various states of charge.

4.2 Nature of Redox Processes in LMNOF Materials

To elucidate the extent to which $\mathrm{Mn^{2+/4+}}$ and oxygen redox contribute to the observed electrochemical capacity, *ex-situ* acid titrations were conducted using TiMS to analyze DRX cathodes extracted throughout the first charge. Specifically, a pristine cathode containing the as-synthesized DRX material along with cathodes extracted after charging to 4.4 V, 4.6 V, and 4.8 V were studied. During TiMS, any oxidized oxygen species present in the bulk of the DRX material will dissolve into the acid solution where they will undergo a disproportionation reaction to yield $\mathrm{O_2}$ gas and $\mathrm{H_2O}$ [38, 39]. This disproportionation reaction will yield 1 mole of $\mathrm{O_2}$ gas for every 4 moles of electrons extracted during oxidation of the oxide lattice, as described in Section S1 and demonstrated in previous publications [28, 23]. Using the TiMS system, the total amount of $\mathrm{O_2}$ gas evolved from each extracted cathode during acid titration was quantified. Using the stoichiometry associated with the oxygen disproportionation reaction, the amount of $\mathrm{O_2}$ gas evolved was then used to calculate the extent of oxide oxidation and thereby the charge capacity associated with bulk oxygen redox. The total capacity extracted from each electrode, along with the oxygen redox capacity determined by TiMS, were then used to back-calculate the average Mn oxidation state in each cathode according to the composition of each material. The results of this analysis are shown in Figure 2. This analysis relies on the assumption that all capacity comes from either Mn or oxygen redox. While a small amount of capacity is inevitably contributed by the irreversible formation processes studied herein, we expect that the error introduced by this assumption is small relative to the large capacity associated with the bulk redox processes [23]. This expectation is further supported by the scale of the degradation reactions observed throughout the rest of this study, which remains small relative to the scale of the bulk electrochemical reactions.

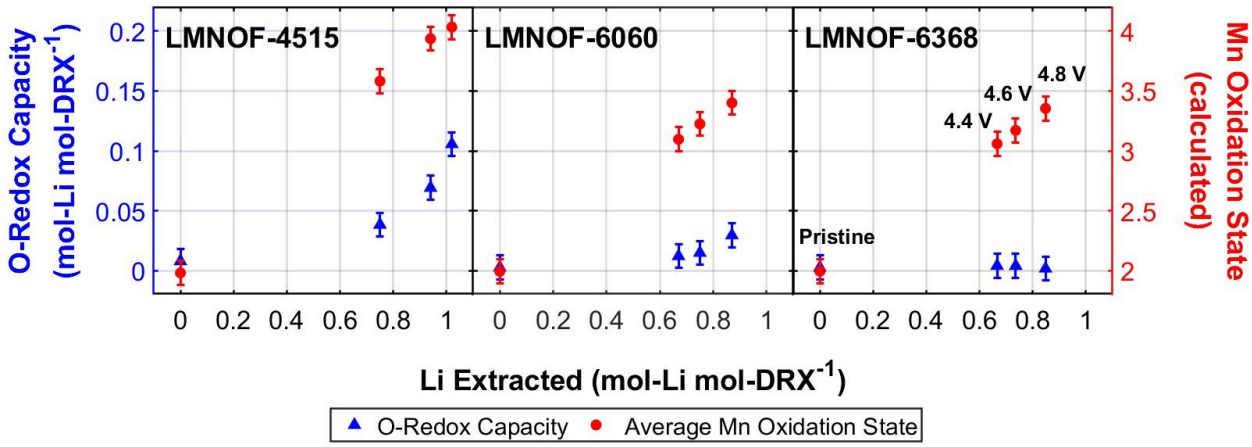

Figure 2: Bulk capacity accounting analysis for LMNOF materials. The pristine sample is a pristine DRX electrode and the remaining samples are DRX electrodes charged to the listed cutoff voltage. Charging consisted of a constant current charge at 0.1 Li hr^{-1} to the listed cut-off voltage followed by a potentiostatic hold at the cut-off voltage until the current decayed to 0.01 Li hr^{-1}. After the potentiostatic hold, the cells were allowed to rest on open circuit. Data labels are included only for LMNOF-6368, but the order of the data points (in the horizontal direction) with regards to electrode condition is the same for the other two materials.

The results in Figure 2 demonstrate the mixed contributions of $Mn^{2+/4+}$ and oxygen redox to the charge capacity extracted from the LMNOF materials. Below 4.4 V, $Mn^{2+/4+}$ redox clearly dominates in LMNOF-4515 because the Mn oxidation state rises linearly with capacity while very little oxygen redox occurs. Above 4.4 V, oxygen redox begins to dominate as the Mn oxidation state approaches 4+. In comparison, the majority of charge compensation in LMNOF-6060 appears to come from Mn redox throughout the entire first charge, with very small contributions from oxygen redox above 4.4 V. The average Mn oxidation state in LMNOF-6060 reaches about +3.4, indicating that the Mn redox couple is not fully exhausted during charging. Finally, in the case of LMNOF-6368, the entirety of charge compensation during the first charge comes from $Mn^{2+/4+}$ oxidation, with no measurable oxygen redox taking place. At the top of charge, the average Mn oxidation state in LMNOF-6368 is about +3.4. In total, the amounts of Li deintercalated from the cathodes extracted at 4.8 V are 1.02 mol Li/mol DRX for LMNOF-4515, 0.87 mol Li/mol DRX for LMNOF-6060, and 0.85 mol Li/mol DRX for LMNOF-6368. Based on prior replicate experiments, the estimated variability in the amount of Li extracted during charging is ~ 0.02 Li hr^{-1}.

Interpreting the bulk redox contributions from the LMNOF materials relies on an understanding of how much Li extraction per formula unit DRX can be charge compensated by $Mn^{2+/4+}$ oxidation. Increasing fluorination in the LMNOF materials comes with a corresponding increase in Mn content. Because Mn undergoes a 2 electron oxidation from Mn^{2+} to Mn^{4+}, 2 Li may be extracted for every Mn that is fully oxidized. In LMNOF-4515, Mn oxidation can therefore theoretically account for 0.9 mol Li/mol DRX. In LMNOF-6060, on the other hand, there is exactly enough Mn to provide charge compensation for the removal of the entire amount of Li (1.2 mol Li/mol DRX). Finally, in LMNOF-6368, there is more Mn than is needed to provide charge compensation for the entirety of the Li. This stoichiometry implies that it is impossible to drive complete oxidation to Mn^{4+} via delithiation alone in LMNOF-6368.

Comparing the amount of oxygen redox occurring in these three materials demonstrates the role of fluorination in tuning the bulk redox processes in DRX materials. Increasing the extent of fluorination from 7.5% (LMNOF-4515) to 30% (LMNOF-6060) leads to a significant decrease in the capacity provided by oxygen redox, and further increasing the extent of fluorination to 33.75% (LMNOF-6368) diminishes the oxygen redox process to the point that it does not supply any appreciable capacity. This observation is consistent with previous findings in similar DRX materials that fluorination suppresses oxygen redox [23, 18]. As explained earlier, an increase in fluorine content is accompanied by an increase in Mn content, raising

the theoretical Mn capacity. This increase in Mn content is likely to reduce the demand placed on oxygen redox to provide charge compensation at the end of charge. Another factor that may contribute to the effect of fluorination on oxygen redox is the amount of Li-O-Li environments present in the DRX material during charging, which will decrease as the lattice oxygen is increasingly replaced with fluorine.

Despite the associated increase in Mn content, the total Li extracted upon charging to 4.8 V decreases slightly with increasing fluorination. One potential explanation for the decreased capacity is that increasing fluorination reduces the amount of Li that is extractable during charge. Many reports have argued that strongly attractive Li-F interactions give rise to short-range order (SRO) that promotes the coordination of Li to F. SRO can impact Li transport in DRX materials, which occurs through a network of percolating tetrahedral sites with zero transition metals in the face-sharing octahedral sites (0-TM sites). Prior investigations have shown that the SRO brought about in DRX materials by fluorination may in some cases disrupt the network of 0-TM sites, thereby limiting the amount of extractable Li [12]. Furthermore, increasing fluorine content may also increase the amount of Li coordinated to a high number of F anions, an effect referred to as Li gettering. Li in high F-coordination environments would require a potential greater than 4.8 V for deintercalation during charge due to strong binding to the F anions, so an increase in the amount of Li in high F-coordination environments could also limit the amount of Li that is extractable within the electrolyte stability voltage window [40]. As a consequence of the decreasing extractable Li and increasing Mn content, the average Mn oxidation state at the top of charge therefore decreases with increasing fluorine content, reflecting decreased fractional utilization of the Mn redox reservoir. An additional factor that may play a role in the observed effects of fluorination is reduced lattice covalency due to poorer metal-ligand orbital overlap [41, 42]. Reduced lattice covalency would lower the energy of antibonding TM-d-states, potentially impeding complete utilization of the transition metal redox reservoir.

4.3 Evolution of Surface Carbonates During Cycling

Lithium carbonate commonly exists in small quantities as an impurity on the surface of all Li-ion cathode active materials, including layered oxides and DRX materials, either as residual precursor from synthesis or as a product of exposure to CO_2 during material handling and processing [43, 28]. This species is referred to as native carbonate, referring to the fact that it is present on the as-synthesized material before exposure to the electrolyte. Separately, additional carbonate-like species can form on the surface of DRX materials during cycling as a result of degradation of the electrolyte [23, 28, 38]. These surface carbonate species, both native and electrolyte-originating, may decompose to evolve gaseous CO_2 due to either electrochemical oxidation or reaction with acidic electrolyte degradation products [28, 43]. In addition to the reactions involving these various surface carbonate species, CO_2 can also arise from oxidative electrolyte degradation at the cathode surface [23, 28]. While CO_2 evolution can be monitored *in-situ* using DEMS, it is not possible to decouple electrolyte degradation from surface carbonate degradation as sources of CO_2 using *in-situ* gas evolution data alone.

To more accurately evaluate the specific processes underlying the observed CO_2 evolution, *in-situ* DEMS analysis of CO_2 evolution was paired with *ex-situ* TiMS analysis of surface carbonate species on DRX samples extracted from DEMS cells throughout the first charge. Upon exposure to acid during TiMS, any carbonate-like species on a DRX sample will decompose in the acidic solution to yield CO_2 as described in Section S1. For each DRX material, CO_2 evolution was measured by TiMS during acid titration of a pristine cathode and cathodes charged to 4.4 V, 4.6 V, and 4.8 V. For the charged samples, charging consisted of a constant current charge at 0.1 Li hr^{-1} to the selected cutoff voltage followed by a potentiostatic hold at the cutoff voltage until the current decayed to 0.01 Li hr^{-1}. For each titration, the CO_2 evolution measured by TiMS was quantified and used to determine the amount of surface carbonate species present on each DRX sample. Under this mode of analysis, surface carbonate decomposition should result in CO_2 evolution during DEMS accompanied by a corresponding decrease in the amount of surface carbonate measured subsequently by TiMS. In contrast, electrolyte degradation should result in CO_2 evolution during DEMS with either increasing or constant amounts of surface carbonate as measured by TiMS. With this insight, the change in surface carbonate measured by TiMS along with the *in-situ* CO_2 data measured by DEMS can be used to evaluate the extents to which surface carbonate decomposition and electrolyte degradation occur between each cut-off voltage.

The DEMS CO_2 evolution data and corresponding TiMS surface carbonate measurements together reveal

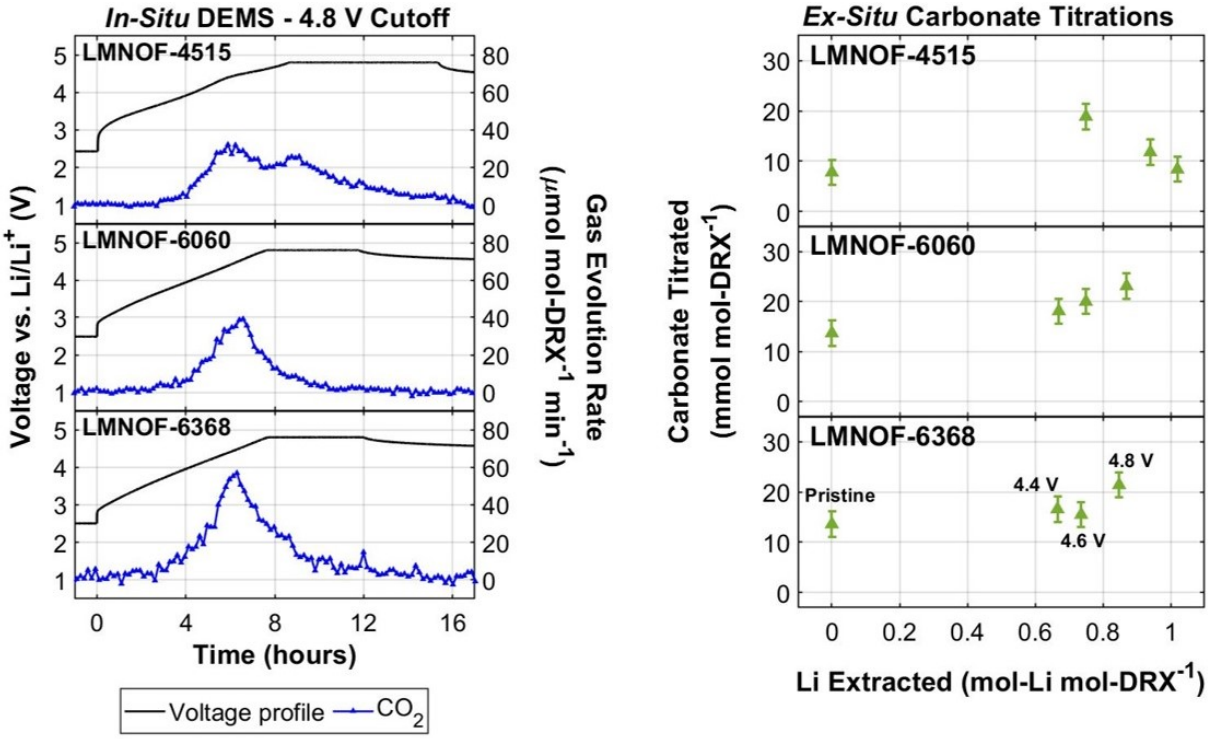

Figure 3: *In-situ* CO_2 evolution during charging of LMNOF materials to 4.8 V vs. Li/Li^+ as measured by DEMS (left) and surface carbonate species on LMNOF materials as measured by *ex-situ* TiMS (right). For electrode titrations, the pristine sample is a pristine DRX electrode and the remaining samples are DRX electrodes charged to the listed cutoff voltage. Charging consisted of a constant current charge at 0.1 Li hr^{-1} to the listed cut-off voltage, followed by a potentiostatic hold at the cut-off voltage until the current decayed to 0.01 Li hr^{-1}. After the potentiostatic hold, the cells were allowed to rest on open circuit. Data labels are included only for LMNOF-6368, but the order of the data points (in the horizontal direction) with regards to electrode condition is the same for the other two materials.

the processes underlying CO_2 evolution in the cell. The DEMS CO_2 evolution results for each material when charged to 4.8 V, along with the carbonate titration results for each cathode studied, are shown in Figure 3. The remaining CO_2 evolution results obtained by DEMS for the cathodes charged to 4.4 V and 4.6 V are shown in Figure S1. Furthermore, the cumulative CO_2 evolution results from each DEMS experiment are given in Table S1 and the amounts of surface carbonate measured by TiMS for each cathode are given in Table S2. During initial charging to 4.4 V, there is a large amount of CO_2 evolution from all three materials that reaches a maximum at 4.4 V. The quantity of CO_2 evolved is largest from LMNOF-6368, whereas the quantity evolved is slightly smaller for LMNOF-4515 and LMNOF-6060. Concurrently, there is an increase in the carbonate-like species on the surface of all three DRX materials, which is greatest for LMNOF-4515 and slightly smaller for LMNOF-6060 and LMNOF-6368. These results indicate that there is significant electrolyte degradation leading to CO_2 evolution as well as carbonate deposition on the cathode surface during initial charging to 4.4 V.

During continued charging of LMNOF-4515 from 4.4 V to 4.8 V, a second peak of CO_2 evolution that reaches a maximum at the start of the 4.8 V voltage hold is observed. LMNOF-6060 and LMNOF-6368, in contrast, do not display this secondary CO_2 evolution peak. Instead, the CO_2 evolution rate decreases monotonically to zero after the 4.4 V CO_2 peak for LMNOF-6060 and LMNOF-6368. Interestingly, this second peak of CO_2 evolution coincides with a dramatic decrease in surface carbonate content measured using TiMS for LMNOF-4515. As can be seen in Figure 3, the amount of surface carbonate decreases consistently from 4.4 V to 4.8 V for LMNOF-4515 whereas it continues to increase for LMNOF-6060 and LMNOF-6368.

These observations therefore indicate that there is significant surface carbonate decomposition occurring on LMNOF-4515 during charging from 4.4 V to 4.8 V, leading to CO_2 evolution and a decrease in the amount of surface carbonate. In contrast, such surface carbonate oxidation does not occur to a significant extent from LMNOF-6060 or LMNOF-6368, causing the observed lack of CO_2 evolution and steady rise in surface carbonate.

The observed differences in electrolyte degradation and surface carbonate oxidation reveal the important role of DRX surface composition in controlling interfacial reactivity. The lack of surface carbonate oxidation above 4.4 V from LMNOF-6060 and LMNOF-6368, despite the presence of carbonate species, indicates that there is some degree of protection or stabilization of the surface carbonate species. This observed difference in the oxidative stability of surface carbonate species across the three DRX materials suggests that the increasing fluorination and the corresponding increase in Mn/Nb ratio plays some role in protecting or otherwise stabilizing carbonate-like species on the surface of DRX cathodes at high voltages.

4.4 Outgassing Comparison during Early Cycling

To monitor the extent and persistence of various important degradation reactions involving DRX materials, DEMS outgassing experiments were conducted during cycling of all three LMNOF materials for four full cycles. For these experiments, all materials were charged to an upper cut-off voltage of 4.8 V vs. $Li^{0/+}$ and discharged to a lower cut-off voltage of 1.5 V vs. $Li^{0/+}$. During cycling, the evolution of CO_2, O_2, and H_2 was monitored and quantified. To ensure that electrolyte depletion does not influence the interfacial degradation processes, a large excess of electrolyte (60 μL cm^{-2}) was used in all DEMS cells. The results of these experiments are displayed in Figure 4, and cycle-to-cycle cumulative gas evolution quantities are given in Table S3.

O_2 evolution is only observed to a very minor extent at the end of the first charge of LMNOF-4515. The lack of O_2 evolution from LMNOF-6060 and LMNOF-6368 indicates that increasing fluorine content suppresses O_2 evolution, a finding that is consistent with previous studies [22, 23]. This observation is also supported by the bulk capacity accounting analysis presented earlier in Section 4.2, which showed that increasing fluorination reduces the extent of bulk oxygen redox occurring in DRX materials. O_2 evolution occurs as a result of irreversible oxidation of the DRX oxyfluoride surface. Consequently, O_2 evolution is generally observed from lithium-excess oxide or oxyfluoride cathode materials at high states of delithiation wherein significant oxygen redox must occur. By reducing the extent to which the oxide lattice is oxidized during charging, fluorination also reduces the driving force for O_2 evolution. Furthermore, the lack of O_2 evolution from LMNOF-4515 on subsequent cycles indicates that the surface of the material forms a densified outer layer that passivates the material from additional O_2 evolution. A more detailed analysis of the O_2 from the DRX materials is conducted in Section S4, in which the O_2 evolution during a constant current charging to 4.8 V followed by a long potentiostatic hold at 4.8 V is presented.

H_2 evolution is observed at potentials above 4 V during high voltage cycling of all three DRX materials throughout all four cycles. Notably, more H_2 evolution is observed from the cells containing LMNOF-6060 and LMNOF-6368 than from the cell containing LMNOF-4515, and the amount of H_2 evolved attenuates only slightly from cycle to cycle for each material. Significant H_2 evolution is not common during comparable cycling of other Mn and Nb-containing DRX materials with the same electrolyte, eliminating the possibility that H_2 evolution occurs due to residual moisture in the electrolyte [23]. Instead, H_2 evolution is expected to arise from a three step process. First, high-voltage electrolyte oxidation at the DRX surface forms protic degradation products. Second, the protic degradation products diffuse across the electrolyte to the anode surface. Third, the protic electrolyte degradation products are reduced at the anode surface to form H_2. Metzger et al. previously demonstrated the occurrence of this process with NMCs by using a specialized two-compartment DEMS cell to demonstrate that H_2 evolution does not occur when diffusion of protic species is blocked [44]. Additionally, several other studies have demonstrated that electrolyte oxidation leads to the formation of protic degradation products, supporting the proposed first step of this process [45, 46, 47]. Moreover, the third step of this process is supported by experiments presented in Section S5, in which delithiated lithium iron phosphate was used in place of Li metal to show that no H_2 occurs when the counter-electrode potential is high enough to prohibit reduction of protic species. Although the nature of this protic electrolyte degradation product remains unclear, we suspect that either of the carbonate solvents in the electrolyte are oxidized to form some sort of organic species like an alcohol or carboxylic acid.

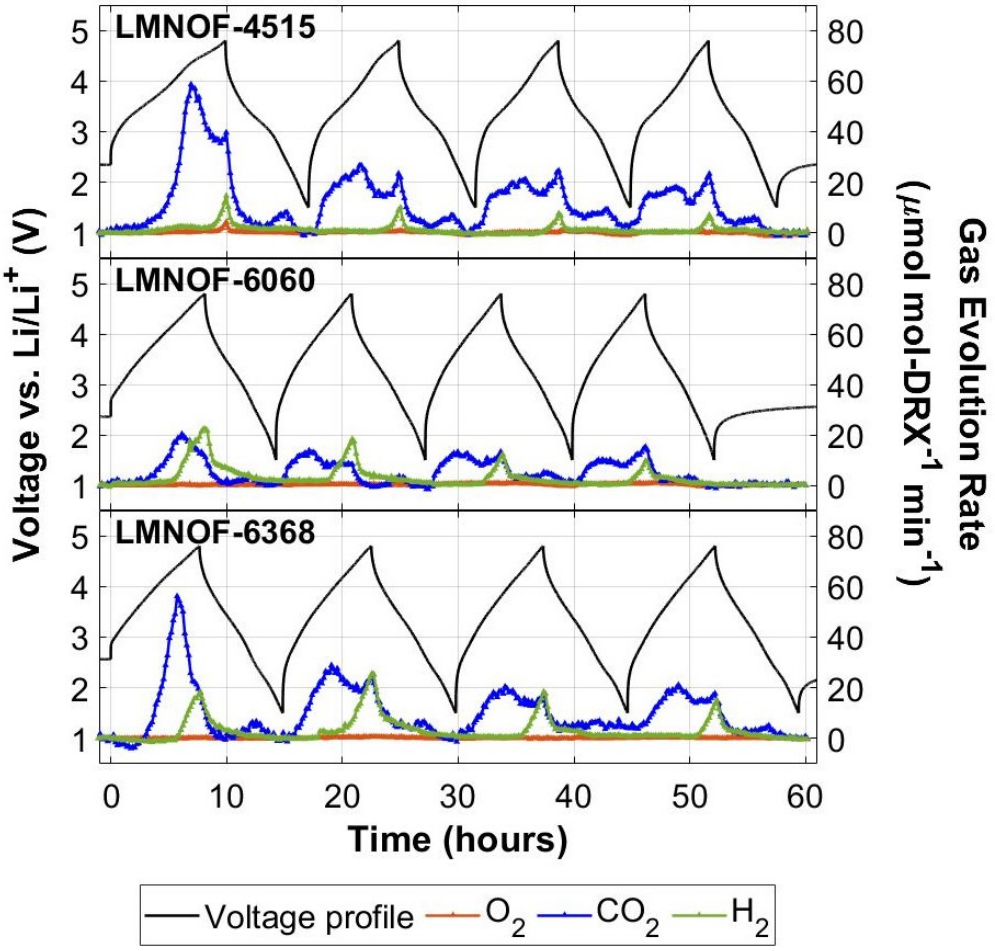

Figure 4: DEMS gas evolution results from LMNOF DRX materials during the first four cycles. Cycling consisted of charging to 4.8 V and discharging to 1.5 V at a constant current of 0.1 Li hr^{-1}. After the fourth cycle, the cells were allowed to rest on open circuit.

Given that H_2 evolution is not typically observed for other related DRX materials, something characteristic to the materials studied herein must lead to elevated interfacial reactivity that drives the formation of acidic electrolyte degradation products. The materials studied in this work were synthesized via high energy ball milling to access extremely high levels of fluorination, giving rise to a high specific surface area and surface damage. In contrast, the DRX materials studied in previous reports in which H_2 was not observed were produced by conventional solid-state synthesis.[23, 28] We hypothesize that the morphology and surface composition of the ball-milled materials leads to an elevated interfacial reactivity, driving the electrolyte degradation processes underlying high voltage H_2 evolution. This hypothesis is further supported by the fact that the milling time was greater for LMNOF-6060 (18 hours) and LMNOF-6368 (20 hours) than for LMNOF-4515 (10 hours), potentially causing more surface damage and explaining the elevated H_2 evolution from the cells containing LMNOF-6060 and LMNOF-6368.[18] These results highlight the importance of material synthesis and particle morphology. Finally, with regard to the slightly decreasing rates of H_2 evolution from cycle to cycle, it is likely that CEI formation and other modes of interfacial passivation cause the cathode surface becomes less reactive towards the electrolyte.

Finally, all three materials exhibit CO_2 evolution during all cycles. On the first charge, in the case of LMNOF-4515, the CO_2 evolution occurs in two separate peaks, the first reaching its maximum around 4.4 V and the second reaching its maximum at 4.8 V (top of charge). During the first charge of LMNOF-6060 and

LMNOF-6368, on the other hand, only the first peak of CO_2 evolution at 4.4 V is observed. As discussed previously in Section 4.3, the CO_2 evolution peak from all materials at 4.4 V is likely caused by electrolyte degradation while the secondary CO_2 evolution peak from LMNOF-4515 at 4.8 V is likely caused by surface carbonate decomposition. On subsequent charges, the CO_2 evolution profiles for all three materials exhibit a similar pattern featuring a broad peak around ∼4.4 V and a sharp peak around 4.8 V, much like the CO_2 evolution from the first cycle of LMNOF-4515. Based on this similarity to the first cycle CO_2 evolution from LMNOF-4515, it is likely that the CO_2 evolution on subsequent charges from all three materials is driven by the same processes of lower-voltage (∼ 4.4 V) electrolyte degradation and higher-voltage (∼ 4.8 V) surface carbonate decomposition. Interestingly, the CO_2 evolution occurring at 4.8 V attributed to surface carbonate decomposition regularly coincides with H_2 evolution for all three materials, suggesting that the potentially acidic electrolyte degradation products that are reduced to form H_2 may also react at the cathode surface to degrade carbonate species. In addition to the CO_2 evolution observed during charging, a small amount of CO_2 evolution was also observed at the bottom of discharge (<3 V) for all three materials for each cycle. We note that this observation is surprising, as CO_2 is commonly considered an oxidation product of degradation at the cathode surface rather than a reduction product. While the processes underlying this CO_2 during discharge remain unknown, it is likely that the CO_2 originates from some type of electrolyte degradation. A follow-up study aims to further investigate this low-voltage activity and its effect on electrolyte degradation, and the results of this study will be summarized in a subsequent report. Finally, the total amount of CO_2 evolved during charge decreases from cycle to cycle for all three materials, suggesting a gradual attenuation in interfacial reactivity as the cathode surface becomes progressively more passivated.

Considering the effects of the observed degradation provides insight into the manner in which performance decay occurs in DRX cells. O_2 evolution leaves behind an oxygen-depleted, cation-densified outer layer that cannot be re-intercalated and instead creates a barrier to Li transport.[48, 22] The processes that underlie H_2 evolution cause both electrolyte depletion and formation of acidic species that may degrade other cell components. For example, acidic species formed at the cathode surface may drive secondary degradation processes like dissolution of transition metals, hydrolysis of $LiPF_6$, reaction with the separator, and decomposition of passivating species like Li_2CO_3 and LiF on the surface of either electrode .[49, 50, 51, 46] Finally, the electrolyte degradation process resulting in CO_2 evolution inevitably leads to depletion of the electrolyte and deposition of insulating degradation products on the cathode surface [43, 28].

4.5 Fluoride-Scavenging DEMS Analysis of Fluorine Dissolution

Another interfacial degradation process of great importance is dissolution of DRX-originating fluorine at the cathode-electrolyte interface. Previous studies have shown that lattice fluorine dissolves from the surface at high voltages [23]. To learn more about the fluorine dissolution process, a modified DEMS technique was used to monitor *in-situ* the dissolution of DRX-originating fluorine into the electrolyte. By allowing the measurement of gaseous species formed by any reaction occurring within the cell, DEMS can be paired with various additives that drive gas-evolving reactions to provide indirect measurements of other processes. Tris(trimethylsilyl) phosphate (TMSPa) is an electrolyte additive that will react with dissolved fluoride ions to yield gaseous trimethylsilyl fluoride (Me_3SiF), which can then be detected and measured using DEMS [30, 52]. TMSPa reacts very slowly with solid fluorides, but it reacts much more rapidly with dissolved fluoride in the electrolyte [31]. Furthermore, TMSPa will not abstract fluorine from other fluorine-containing species (i.e. $LiPF_6$, LiTFSI, PVDF) to produce Me_3SiF [52]. Based on these characteristics, we assume that significant Me_3SiF evolution arises only from reaction of TMSPa with dissolved fluoride ions in the electrolyte. Therefore, when DEMS experiments are conducted with electrolyte containing TMSPa, Me_3SiF evolution can be monitored *in-situ* as a signal to represent the formation of dissolved fluoride in the electrolyte. This technique, referred to as fluoride-scavenging DEMS, has been used in previous studies to study dissolved fluoride formation originating from both electrolytes and oxyfluoride cathode materials [23, 30, 52].

While Me_3SiF evolution measured by fluoride-scavenging DEMS signals the formation of dissolved fluoride species in the electrolyte, additional steps must be taken to exclusively study fluorine dissolution from DRX materials. As previously mentioned, TMSPa will react with dissolved fluoride species (i.e. LiF, HF) in the electrolyte. Consequently, fluoride species formed via degradation of commonly used cell components like $LiPF_6$ salt and polyvinylidene fluoride (PVDF) binder may contribute to any observed Me_3SiF during fluoride-scavenging DEMS. To study the dissolution of DRX-originating fluorine exclusively, all other po-

tential sources of fluoride must therefore be eliminated from the cell. For the fluoride-scavenging DEMS experiments conducted in this work, the PVDF cathode binder was replaced with polyethylene (PE) and the $LiPF_6$ electrolyte salt was replaced with LiTFSI. We note that while LiTFSI still contains fluorine, it does not degrade to form fluoride to any significant extent. Indeed, control experiments in which a fluorine-free NMC material is charged in LiTFSI-based electrolyte with TMSPa reveal no significant Me_3SiF evolution, as shown and discussed in Section S6. We therefore conclude that any Me_3SiF evolution observed from cells containing DRX cathodes with PE binder and electrolyte with LiTFSI salt must come from DRX-originating fluorine, allowing us to exclusively study fluorine dissolution from the DRX material.

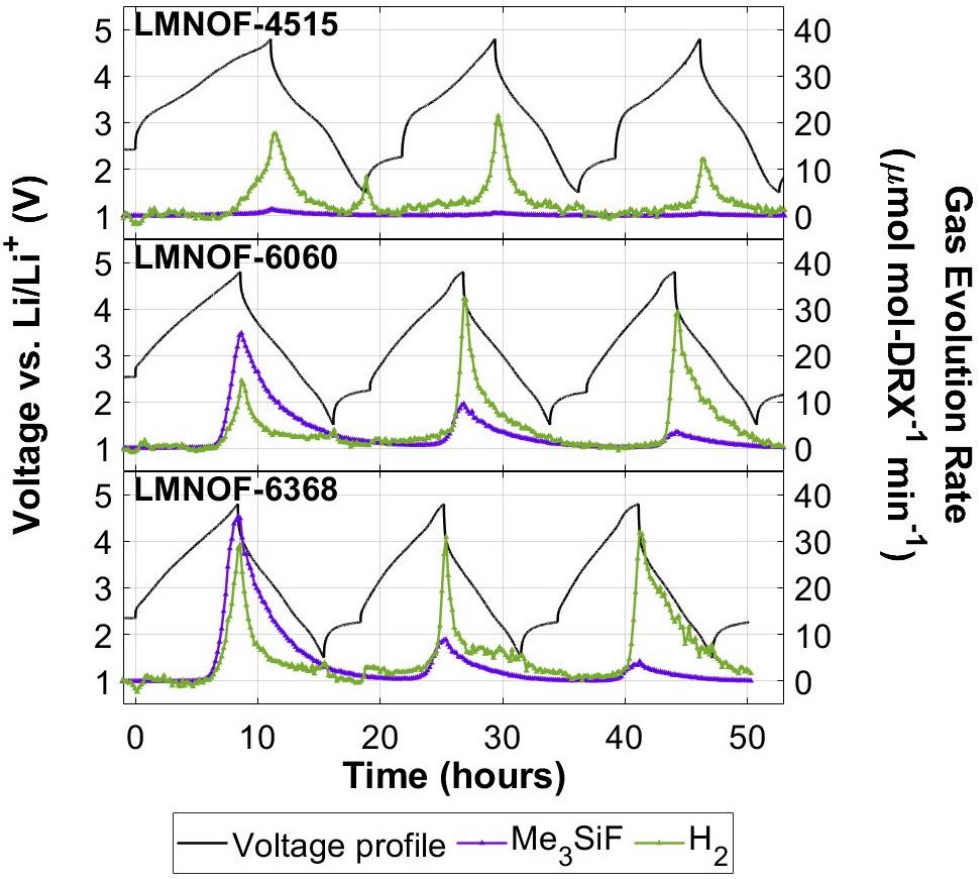

Figure 5: Fluoride-scavenging DEMS results from LMNOF DRX materials during the first three cycles. Each cycle consisted of charging to 4.8 V and discharging to 1.5 V at a constant current of 0.1 Li hr^{-1}. After each discharge, the cells were allowed to rest on open circuit for 2 hours before the next cycle.

To study fluorine dissolution from the set of DRX materials during early cycling, fluoride-scavenging DEMS was conducted for all three materials during the first three cycles with cells containing the aforementioned fluorine-free components. All cathodes were charged to an upper cutoff voltage of 4.8 V and discharged to a lower cutoff voltage of 1.5 V at a constant current rate of 0.1 Li hr^{-1} with a three hour rest after each discharge. The results of the fluoride-scavenging DEMS experiment for each DRX material, including the voltage profile and the gas evolution profiles of Me_3SiF and H_2, are shown in Figure 5. We include H_2 here given the general coincidence of its evolution with that of Me_3SiF. As explained, the observed Me_3SiF evolution serves as an *in-situ* signal for dissolution of DRX-originating fluorine into the electrolyte. Very little Me_3SiF evolution is observed from LMNOF-4515 throughout all three cycles. In contrast, significant Me_3SiF evolution during cycling of both LMNOF-6060 and LMNOF-6368 occurs during charging above ~4.3 V and reaches a maximum at the top of charge (4.8 V). Furthermore, the amount of Me_3SiF

evolved decreases from cycle to cycle. These results show that the dissolution of DRX-originating fluorine occurs from the surface of both LMNOF-6060 and LMNOF-6368, whereas very little fluorine dissolution takes place from the surface of LMNOF-4515. The attenuation in fluorine dissolution from LMNOF-6060 and LMNOF-6368 over cycling, demonstrated by the decreasing extent of Me_3SiF evolution, suggests that a fluorine-depleted region gradually forms near the surface of LMNOF-6060 and LMNOF-6368 during the first few cycles. This fluorine-depleted region is likely to passivate the DRX materials from further fluorine dissolution. The cumulative amounts of Me_3SiF evolved for each material and the corresponding amount of DRX fluorine dissolved are given in Table S4. Importantly, the amount of fluorine dissolved amounts to about 1-2% of the fluorine contained within the DRX material for both LMNOF-6060 and LMNOF-6368.

The voltage dependence of fluorine dissolution process indicates that the underlying reaction is electrochemical in nature. This observation is further supported by the very low solubility of species like LiF in carbonate solvents, suggesting that some sort of electrochemically-driven process must assist in the dissolution of surface-bound fluorine [53]. The dissolution of surface-bound fluorine species may be activated by the electrochemical formation of other reactive intermediate species. Interestingly, the evolution of Me_3SiF shown in Figure 5 appears to generally coincide with H_2 evolution. Most notably, the onset of Me_3SiF evolution and H_2 evolution occur very closely to one another for LMNOF-6060 and LMNOF-6368 for each cycle. As explained earlier, H_2 evolution occurs due to the formation of protic electrolyte degradation products on the surface of the cathode and subsequent reduction of the protic species to form H_2 at the Li metal anode. Based on these observations, one possible explanation for the electrochemical dependence of fluorine dissolution and the enhanced solubility of the fluoride species in the electrolyte is that reactive acidic electrolyte degradation products assist in the dissolution of surface-bound fluorine. Previous studies have shown the role of acidic species in driving dissolution of TMO cathode materials, wherein protic species abstract oxide to form water as well as dissolved lithium and/or transition metals [54, 55, 49]. An analogous reaction, in which protons or protic species abstract surface fluorine to form HF and dissolved lithium and/or transition metals, could be the process underlying the observed fluorine dissolution. Surface dissolution in this manner would inevitably lead to a loss of cathode capacity and may also lead to subsequent reaction of dissolved fluoride species (i.e. HF) with other cell components. This observation provides an important example of how initial electrolyte degradation may cause a cascade of subsequent degradation reactions via the formation of reactive intermediate species like protic electrolyte degradation products.

While the extent of fluorine dissolution does appear to trend with the fluorine content of the DRX material, the stark contrast between the fluorine dissolution from LMNOF-4515 and that from LMNOF-6060 and LMNOF-6368 suggests that the trend is not linear with bulk fluorine content. This strong difference suggests that there is a heightened reactivity of the surface fluorine in the case of LMNOF-6060 and LMNOF-6368, which may indicate the existence of a threshold value for the fluorine content below which the fluorine is largely stable on the DRX surface. Another possible explanation for this elevated reactivity relating to DRX composition is that the increasing Mn content and decreasing Nb content associated with increasing fluorination lowers the stability of fluorine on the DRX surface. Finally, another alternative explanation is that the extended milling times required to synthesize LMNOF-6060 (18 hours) and LMNOF-6368 (20 hours) relative to that of LMNOF-4515 (10 hours) induces additional surface damage and smaller particle size, leading to more fluorine dissolution from the DRX material.

4.6 ICP Analysis of Mn Dissolution

The outgassing observed during cycling of DRX materials demonstrates the various degradation modes that take place at the cathode-electrolyte interface. In particular, the evolution of H_2 indicates that acidic electrolyte degradation products are formed at the cathode surface, as explained in the previous sections. Manganese dissolution is a process known to occur from transition metal oxide materials like spinel $LiMn_2O_4$ at high voltages, and many studies have indicated that acid species formed by high-voltage electrolyte degradation actively drive manganese dissolution. Many of these studies also suggest that Mn dissolves as Mn^{2+}, often first requiring disproportionation of Mn^{3+} to Mn^{2+} and Mn^{4+} or reduction of $Mn^{3+/4+}$ by electrolyte degradation products [56, 55, 54]. Once dissolved, the manganese species are likely to either remain dissolved in the electrolyte or migrate across the electrolyte and deposit on the anode [49]. To further investigate the dissolution processes occurring on the surface of DRX materials, ICP was used to quantify manganese species dissolved in the electrolyte or deposited on the surface of the Li metal counter-electrodes

used during the first charge of the DRX cathodes. Since no other cell components contain manganese, any manganese detected by ICP must be a product of dissolution from the DRX surface.

For each DRX material, the amount of Mn dissolved from the cathode was quantified after three different procedures: rest at open circuit (OCV), charge to 4.0 V, and charge to 4.8 V. For the OCV procedure, the cell was simply allowed to rest at open circuit for 24 hours. For the two charge procedures, charging consisted of a constant current charge at 0.1 Li hr^{-1} to the selected cut-off voltage followed by a potentiostatic hold the cut-off voltage until the current decayed to 0.01 Li hr^{-1}. To control cathode-electrolyte contact time across different procedures, the charged cells were allowed to rest at open circuit until the total time in contact with the electrolyte was 24 hours. For each sample, a propagation of uncertainty analysis was carried out to estimate the error in the calculated amount of Mn dissolution, which results from uncertainty in the cathode loading and the ICP measurement. The results of the Mn dissolution study and corresponding propagation of uncertainty analysis are shown in Figure 6. The Mn dissolution observed from all three samples of LMNOF-4515 was 0.5 mmol-Mn mol-DRX^{-1}, while the Mn dissolution from all three samples of LMNOF-6060 was 0.7 mmol-Mn mol-DRX^{-1}. For both LMNOF-4515 and LMNOF-6060, the Mn dissolution accounts for about $\sim$ 0.1% of DRX Mn. In contrast, for LMNOF-6368, a growing amount of Mn dissolution is observed with increasing cutoff voltage. Slightly more Mn dissolution is observed for LMNOF-6368 from the 4.0 V sample (0.68 mmol-Mn mol-DRX^{-1}, $\sim$ 0.1% DRX Mn) than from the OCV sample (0.53 mmol-Mn mol-DRX^{-1}, $\sim$ 0.08% DRX Mn), and significantly greater Mn dissolution is observed in the 4.8 V charge sample (3.66 mmol-Mn mol-DRX^{-1}, $\sim$ 0.6% DRX Mn).

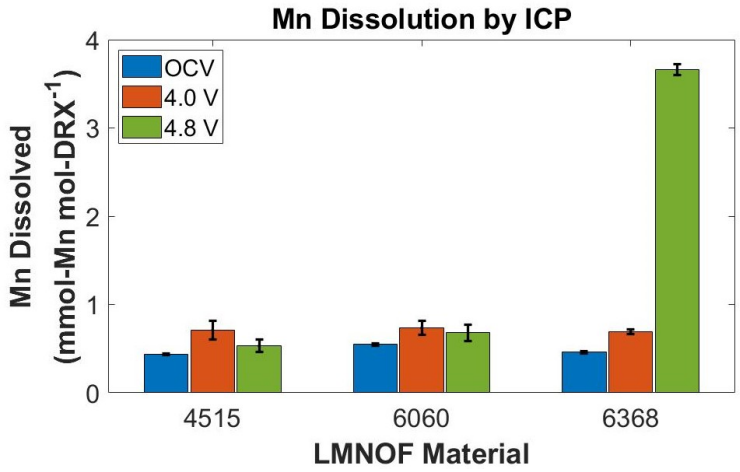

Figure 6: Amount of Mn dissolved from LMNOF materials after an open circuit rest period in the electrolyte (OCV), upon charge to 4.0 V (4.0 V), and charge to 4.8 V (4.8 V). Charging consisted of a constant current charge at 0.1 Li hr^{-1} to the selected cut-off voltage followed by a potentiostatic hold at the cut-off voltage until the current decayed to 0.01 Li hr^{-1}. To control for cathode-electrolyte contact time, all cathodes spent 24 hours in the cell. Error bars are obtained from a propagation of uncertainty analysis to estimate the error contributed by uncertainty in the cathode loading and the ICP measurement.

The small amount of Mn that dissolves from all three materials without any charging may be due to the dissolution of Mn^{2+} species from the DRX surface into the electrolyte in very small quantities. Further, the dramatic increase in Mn dissolution observed from the LMNOF-6368 4.8 V sample suggests that an additional Mn dissolution process sets in during charging of LMNOF-6368 above 4.0 V. The occurrence of additional manganese dissolution from LMNOF-6368 during charging above 4.0 V and lack thereof from LMNOF-4515 and LMNOF-6060 indicates that increasing fluorination and the corresponding shift in Mn/Nb content creates conditions under which Mn dissolution can occur. Given that all three materials were shown to evolve comparable amounts of H_2 evolution during cycling, it is unlikely that this additional high-voltage Mn dissolution from LMNOF-6368 is caused by an increased amount of acidic electrolyte degradation products reacting with the DRX surface. Instead, one potential explanation for the high-voltage Mn dissolution from LMNOF-6368 is that the average Mn oxidation state at the top of charge is lowest in the most fluorinated

DRX material, as demonstrated in Section 2. Assuming that Mn dissolves in the form of Mn^{2+}, a lower average oxidation state (closer to 3+) at the top of charge may enhance Mn dissolution by facilitating Mn^{2+} formation through reduction or disproportionation of Mn^{3+} in LMNOF-6368. In contrast, the Mn in LMNOF-4515 is almost completely in the 4+ state at the top of charge, potentially increasing the barrier to formation of Mn^{2+}. These results provide an important example of how material composition can influence susceptibility towards high-voltage surface dissolution processes. In addition to causing a direct loss of cathode capacity, Mn dissolution is also likely to result in deleterious reaction of dissolved Mn ions at the anode surface, causing additional degradation and loss in cell capacity [49]. The compounded negative consequences associated with Mn dissolution thus make it an important process to study further during high voltage cycling.

4.7 XPS Analysis of Cathode Surface Composition

To further investigate the observed interfacial degradation, XPS was used to study the surface composition of DRX cathodes before and after the first charge to 4.8 V. For each material, the F1s and O1s XPS spectra were measured for both a pristine DRX cathode and a DRX cathode extracted after charging to 4.8 V vs. $Li^{0/+}$. After charging to 4.8 V, the extracted DRX cathode was rinsed with DEC to remove any residual electrolyte or soluble degradation products and subsequently dried under vacuum.

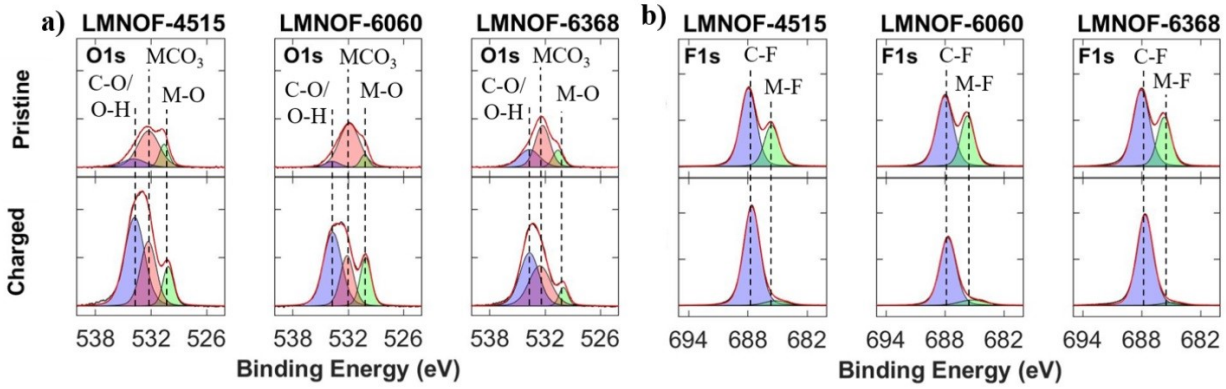

Figure 7: O1s (a) and F1s (b) XPS spectra from LMNOF pristine (top) and charged (bottom) cathodes. Charging consisted of a constant current charge at 0.1 Li hr^{-1} to a 4.8 V cutoff, followed by a potentiostatic hold at 4.8 V until the current decayed to 0.01 Li hr^{-1}. After charging, the cathodes were extracted from their cells, rinsed in DEC to remove residual electrolyte, and dried under vacuum overnight before XPS analysis.

4.7.1 O1s XPS

The O1s XPS spectra for all three materials before and after charging are shown in Figure 7a. All O1s spectra contain three adjacent peaks. The highest energy peak, shown in blue, is assigned to organic C-O groups or O-H groups from impurity species like LiOH and $LiHCO_3$. The middle peak, shown in red, is assigned to metal carbonate (MCO_3) species. Finally, the low energy peak, shown in green, is ascribed to the metal-oxygen (M-O) bonds in the DRX lattice. These peak assignments are consistent with those of several previous studies [57, 58]. Before charging, the pristine cathodes have small contributions from the C-O/O-H peak and the M-O, and the largest contribution is from the metal carbonate group. This measurement suggests that the pristine cathode surface is initially dominated by metal carbonate species, although these carbonates do not completely cover the DRX surface such that the M-O signal from the DRX lattice is also observed. Additionally, the small contribution from the C-O/O-H peak before charging may originate from the O-H bonds in impurity species like LiOH or $LiHCO_3$. Based on the NMR results presented in Section 4.8, the amount of these O-H containing species must be very small (< 1wt%). After charging, the

O1s spectra is instead dominated by the C-O/O-H peak, whereas the metal carbonate peak and the metal oxide peak have smaller but still detectable contributions. The growth of the C-O/O-H peak is likely to be caused by deposition of organic species containing C-O groups on the DRX surface during charging, while the decrease in signal from the metal carbonate species suggests that native metal carbonate species are partially decomposed. The organic species that dominate the surface after charging are likely to be solvent-derived electrolyte degradation products, consistent with the extensive electrolyte degradation observed earlier by DEMS (Section 4). Furthermore, the partial but incomplete decomposition of the metal carbonate species agrees with the findings of the carbonate decomposition studies conducted using DEMS and TiMS (Section S1), demonstrating that some metal carbonate species remain after the first charge. Finally, the retained signal from the M-O peak after charging indicates that the metal oxide of the DRX lattice is not completely buried by the cathode-electrolyte interface (CEI) layer.

4.7.2 F1s XPS

The F1s XPS spectra for all three materials before and after charging, all of which contain two adjacent peaks, are shown in Figure 7b. The higher-energy peak, shown in blue in each spectrum, is attributed to the C-F groups in the PVDF binder [59]. Meanwhile, the lower-energy peak shown in green in each spectrum is attributed to metal-fluorine (M-F) bonds in the DRX lattice [60, 61]. For all three materials, the M-F peak stands out clearly in the pristine sample. In contrast, the M-F peak for all three charged samples is faint, suggesting a decrease in fluorine content near the surface of the DRX materials. The decrease in M-F species after the first charge indicates that a loss of fluorine occurs and/or a thick fluorine-free CEI layer is deposited on the surface of the DRX material. Based on the retained signal from the DRX lattice oxide in the O1s spectra after charging, the CEI layer is not expected to be thick enough to fully mask the signal from the DRX anion lattice underneath. Consequently, the disappearance of the M-F peak in the F1s spectra for all three materials is likely to be caused by a loss of fluorine from the DRX surface during the first charge, consistent with the dissolution of DRX originating fluorine observed in the fluoride-scavenging DEMS experiments. It is important to note that the difference in magnitude of fluorine dissolution between materials observed in the fluoride-scavenging DEMS experiments is not captured by these XPS experiments, which show similar extents of fluorine loss for all three materials. This discrepancy is likely to be caused by the fact that the fluoride-scavenging DEMS cells employed a LiTFSI-based electrolyte whereas the cells used for to prepare the cathodes for XPS employed a $LiPF_6$-based electrolyte. As documented in previous reports and demonstrated further in Section S8, high-voltage cycling with a $LiPF_6$-based electrolyte may result in elevated dissolution of DRX-originating fluorine relative to comparable cycling in a LiTFSI-based electrolyte [23]. The elevated degradation in $LiPF_6$-based electrolyte is likely to be driven by the tendency of the salt anion to form reactive species like HF that are in turn capable of causing DRX dissolution. It is therefore likely that the thickness of the outer fluorine-depleted region formed on the surface of all three DRX materials when cycled in $LiPF_6$-based electrolyte approaches or exceeds the penetration depth of the XPS, causing the M-F peak to nearly disappear for each material. This result highlights the utility of the fluoride-scavenging DEMS results, where more fluoride dissolution is clearly observed with increasing DRX fluorination.

4.8 Solid State NMR of DRX Materials

To further characterize the composition of the DRX cathode materials before and after charging, ^{7}Li and ^{19}F NMR spectra were recorded on LMNOF-4515, LMNOF-6060, and LMNOF-6368 electrodes in the pristine state and after being charged to 4.8 V at a rate of 0.1 Li hr^{-1} followed by a potentiostatic hold at 4.8 V until the current decayed to 0.01 Li hr^{-1} (Figures S6 and Figure S7, respectively).

4.8.1 ^{7}Li NMR

^{7}Li NMR spectra show across all samples a broad and asymmetric line shape spanning a frequency range from 500 to −200 ppm with spinning sidebands on both sides (Figure S6). This broad line shape is attributed to the various local Li environments found within the disordered structure of LMNOF electrodes. This attribution is further supported by the fully isotropic ^{7}Li spectrum (projected magic angle turning phase

adjusted sideband separation, pj-MATPASS, in grey shadings in Figure S6) that highlights a distribution of Li chemical shifts and environments in each LMNOF electrode.

No significant line shape difference is found across pristine electrodes, indicating a similar Li distribution in all pristine compositions. On the other hand, when comparing pristine electrodes to their charged counterparts, the latter exhibit a significant decrease in the overall ^{7}Li signal intensity along with a slight increase in line width (around 60 ppm wider). The decrease in ^{7}Li signal intensity is in line with extraction of Li ions during charge. The slight increase in line width can be attributed to (i) an increase in Li disordering within the DRX structure due to prolonged Li extraction and/or (ii) a modification of the paramagnetic interaction between Mn unpaired electron and ^{7}Li nuclear spin due to the oxidation of Mn ions.

Finally, no sharp signal with an extensive sideband pattern centered at 0 ppm can be observed in the ^{7}Li NMR spectrum, indicating that no significant amount (less than a couple of percent by weight) of Li-based diamagnetic impurities (e.g. LiF or Li_2CO_3) can be detected in these LMNOF electrodes by NMR. This finding is consistent with the amounts of surface carbonate species as measured by acid titration, which are consistently in the range of 1-2% by weight (see carbonate titration results for pristine materials in Figure 3). Furthermore, the minimal amount of Li-based diamagnetic impurities further supports the assumed composition of the ball-milled DRX materials.

4.8.2 ^{19}F NMR

The ^{19}F NMR spectra of pristine LMNOF electrodes are composed of two signals centered around –95 ppm and –190 ppm along with their spinning sidebands on both sides (Figures 8 and S7, top). Since no sharp signal can be detected standing out from the broader DRX signal at –204 ppm, these materials do not contain significant quantities of residual LiF used in the synthesis of LMNOF materials.

The most intense signal at –95 ppm is attributed to the main resonance of $-CF_2-$ in PVDF polymer used as a binder in the LMNOF electrodes [62]. It is worth mentioning that in the LMNOF electrodes, the PVDF signal observed at –95 ppm is overlapping with a significant portion of the LMNOF line shape and only part of the DRX ^{19}F resonance remains visible around –190 ppm (see ^{19}F spectra in top panel of Figure 8). A ^{19}F spin-echo spectrum recorded on the carbon-coated LMNOF-6368 active material (without PVDF binder) is shown in Figure 8 (bottom). Here, a wide and asymmetric ^{19}F line shape is visible, spanning a wide frequency range from 100 to –400 ppm along with spinning sidebands on both sides. This line shape is due to the various local F environments found in the disordered structure of LMNOF electrodes and proves the successful integration of F ions within the DRX structure.

Even though the PVDF signal overlaps with a large portion of the ^{19}F LMNOF electrodes line shape, the ^{19}F signal around –190 ppm can still be used to track the evolution of F^- ions within the LMNOF electrodes before and after a prolonged charge at 4.8 V. Since each LMNOF electrode was prepared with the same ratio of active material to binder (60:10 wt:wt), the intensity of the PVDF ^{19}F signal can be used as an internal reference to normalize the intensity of all ^{19}F spectra (Figure 8, Pristine and Charged, and Figure S7). It is clear that the intensity of the -190 ppm signal increases with the amount of F in the pristine LMNOF cathodes (Figures 8 and S7). Furthermore, as the intensity of the signal for F^- ions within the LMNOF structure increases, the observed chemical shift associated with the F^- ions evolves from –175 ppm (LMNOF-4515) to –185 ppm (LMNOF-6060) and ends up at –198 ppm (LMNOF-6368). This evolution of the ^{19}F chemical shift tends to indicate the formation of larger LiF-rich domains within the LMNOF structure upon increasing fluorine content. As the size of these Li F-rich domains increases, the observed chemical shift moves closer and closer to the isotropic shift of pure LiF at –204 ppm.

After charging, the intensity of the cathode signals centered at about -190 ppm significantly decrease when compared to the -190 ppm signal intensity observed in the spectra collected on the pristine electrodes (Figures 8 and S7). This signal decay upon charging is particularly pronounced for LMNOF-6368 (Figure 8). This change can be explained by either some loss of F^- ions from LiF-rich domains of the DRX structure as Li gets extracted or by cation rearrangements resulting in a greater number of Mn-F bonds in the charged cathode. In the latter case, the strong paramagnetic interactions between ^{19}F nuclei and unpaired electrons from the Mn ions lead to a significantly broader and short-lived ^{19}F NMR signal that is impossible to observe experimentally, resulting in an effective reduction in ^{19}F NMR signal intensity. Finally, after prolonged Li extraction at 4.8 V, the LMNOF-4515 has the least amount of F^- ions left within the DRX structure. LMNOF-6060 and LMNOF-6368 still exhibit a small signal around -190 ppm with the intensity

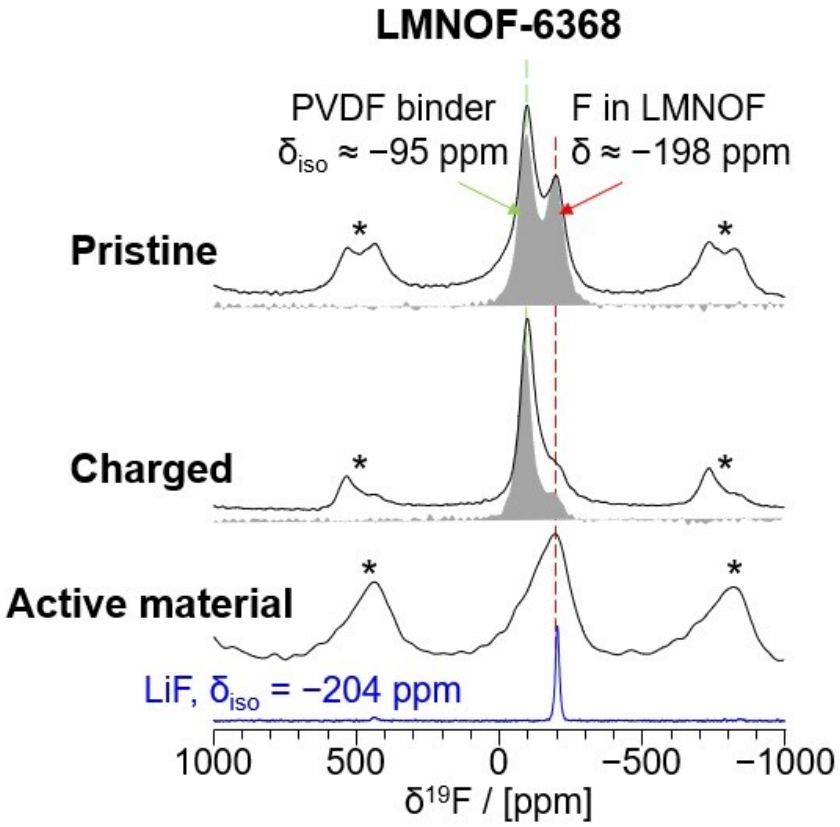

Figure 8: ^{19}F NMR spectra (spin echoes in black and isotropic spectra obtained using the pj-MATPASS sequence in grey shading) recorded on pristine and charged LMNOF-6368 electrodes [35, 36]. For the charged sample, charging consisted of a constant current charge at 0.1 Li hr^{-1} to 4.8 V followed by a potentiostatic hold at 4.8 V until the current decayed to 0.01 Li hr^{-1}. ^{19}F spin-echoes of carbon-coated LMNOF-6368 active material without PVDF binder and pure LiF ($\delta_{iso} = -204$ ppm, in blue) are also shown for comparison with LMNOF-6368 electrodes. ^{19}F NMR spectra were recorded at $B_0 = 2.35$ T with a sample spinning speed $\nu_R = 60$ kHz and spinning sidebands are indicated with asterisks. The isotropic chemical shift of the PVDF binder is highlighted at $\delta_{iso} \approx -95$ ppm with a green dashed line. The most intense ^{19}F signal coming from F^- ions in the LMNOF-6368 structure is highlighted with a red dashed line along with its observed chemical shift $\delta \approx -198$ ppm. The intensity of LMNOF electrodes ^{19}F spectra was normalized so that the PVDF signal of each spectrum reaches the same intensity.

in LMNOF-6368 being the highest. These observations are in line with the fluorine losses observed earlier by *in-situ* fluoride-scavenging DEMS and *ex-situ* XPS, supporting the observation that significant dissolution of lattice fluorine occurs during high-voltage charging.

5 Conclusions

In this work, TiMS was employed to decouple the capacities contributed by $Mn^{2+/4+}$ and oxygen redox during the first charge. This analysis revealed that increasing DRX fluorination from 7.5% to 33.75% deactivates bulk oxygen redox, leaving only $Mn^{2+/4+}$ redox to provide the entirety of the bulk charge compensation. In this context, changing the fluorine content can be seen as a way to tune the extent to which $Mn^{2+/4+}$ and oxygen redox contribute to bulk charge compensation. In addition to studying the bulk electrochemistry of DRX materials, the interfacial degradation occurring on the surface of DRX cathodes during cycling

was also investigated. TiMS was paired with DEMS to reveal that while all three materials undergo low-voltage (~ 4 V) electrolyte degradation during the first charge, only LMNOF-4515 exhibits a high-voltage (~ 4.8 V) surface carbonate decomposition. The DEMS analysis was then extended over the first four cycles to show that O_2 evolution occurs only on the first charge of LMNOF-4515, confirming previous findings that fluorination suppresses high-voltage O_2 evolution. These DEMS experiments also showed that CO_2 and H_2 evolution occur for all three materials to diminishing extents over all four cycles, indicating that multiple routes of degradation associated with high voltage oxidative electrolyte decomposition occur at the DRX surface. Next, a fluoride-scavenging electrolyte additive was introduced into the DEMS cell, revealing *in-situ* the dissolution of DRX-originating fluorine from LMNOF-6060 and LMNOF-6368 at high voltages. Finally, ICP-OES, XPS, and SS-NMR were used to demonstrate the occurrence of several changes in DRX composition including manganese and fluorine dissolution as well as solid organic carbonate deposition.

The results of this study highlight the effects of DRX composition on bulk electrochemistry and interfacial reactivity, ultimately informing material performance in both the short- and long-term. The observed trends indicate that increasing fluorination will suppress oxygen redox, leaving $Mn^{2+/4+}$ redox to provide the majority of bulk charge compensation during cycling. At the same time, increasing fluorination is likely to lead to decreased evolution of O_2 and increased dissolution of Mn and fluorine at high voltages. These observations point to a moderate DRX composition, with fluorine content between that of LMNOF-4515 and LMNOF-6060 ($\sim 10\% - 30\%$), that may have the optimal compromise of these effects. Furthermore, the occurrence of rarely seen electrolyte degradation processes like high-voltage H_2 evolution and CO_2 evolution near the low cutoff voltage during discharge motivates investigation of the high-energy ball-milling DRX synthesis and its effect on interfacial reactivity. Inevitably, the high reactivity brought about by accessing high-voltage redox processes with DRX cathode materials necessitates the development of a cathode-electrolyte interface with improved oxidative stability. Potentially promising routes towards achieving a more stable interface include developing electrolytes with increased resistance towards oxidative degradation as well as passivating the surface of high-energy ball-milled materials via coating or washing.

References

[1] John B. Goodenough and Kyu Sung Park. "The Li-ion rechargeable battery: A perspective". In: *Journal of the American Chemical Society* 135.4 (2013), pp. 1167–1176. ISSN: 00027863. DOI: 10.1021/ja3091438.

[2] M. Stanley Whittingham. "Lithium batteries and cathode materials". In: *Chemical Reviews* 104.10 (2004), pp. 4271–4301. ISSN: 00092665. DOI: 10.1021/cr020731c.

[3] Naoki Nitta et al. "Li-ion battery materials: Present and future". In: *Materials Today* 18.5 (2015), pp. 252–264. ISSN: 18734103. DOI: 10.1016/j.mattod.2014.10.040. URL: http://www.sciencedirect.com/science/article/pii/S1369702114004118%20http://dx.doi.org/10.1016/j.mattod.2014.10.040.

[4] John B. Goodenough and Youngsik Kim. "Challenges for rechargeable Li batteries". In: *Chemistry of Materials* 22.3 (2010), pp. 587–603. ISSN: 08974756. DOI: 10.1021/cm901452z.

[5] Elsa A Olivetti et al. "Lithium-Ion Battery Supply Chain Considerations: Analysis of Potential Bottlenecks in Critical Metals". In: *Joule* 1.2 (2017), pp. 229–243. ISSN: 2542-4351. DOI: https://doi.org/10.1016/j.joule.2017.08.019. URL: http://www.sciencedirect.com/science/article/pii/S2542435117300442.

[6] Kostiantyn Turcheniuk et al. "Ten years left to redesign lithium-ion batteries". In: *Nature* 559.7715 (2018), pp. 467–470. ISSN: 14764687. DOI: 10.1038/d41586-018-05752-3. URL: https://www.nature.com/magazine-assets/d41586-018-05752-3/d41586-018-05752-3.pdf.

[7] Prasant Kumar Nayak et al. "Review on Challenges and Recent Advances in the Electrochemical Performance of High Capacity Li- and Mn-Rich Cathode Materials for Li-Ion Batteries". In: *Advanced Energy Materials* 8.8 (2018), pp. 1–16. ISSN: 16146840. DOI: 10.1002/aenm.201702397.

[8] Jihyun Hong et al. "Review—Lithium-Excess Layered Cathodes for Lithium Rechargeable Batteries". In: *Journal of The Electrochemical Society* 162.14 (2015), A2447–A2467. ISSN: 0013-4651. DOI: 10.1149/2.0071514jes.

[9] Satishkumar B. Chikkannanavar, Dawn M. Bernardi, and Lingyun Liu. "A review of blended cathode materials for use in Li-ion batteries". In: *Journal of Power Sources* 248 (2014), pp. 91–100. ISSN: 03787753. DOI: 10.1016/j.jpowsour.2013.09.052. URL: http://dx.doi.org/10.1016/j.jpowsour.2013.09.052.

[10] Jinhyuk Lee et al. "Unlocking the potential of cation-disordered oxides for rechargeable lithium batteries". In: *Science* 343.6170 (Jan. 2014), pp. 519–522. ISSN: 10959203. DOI: 10.1126/science.1246432. URL: http://science.sciencemag.org/content/343/6170/519.abstract.

[11] R J Clément, Z Lun, and G Ceder. "Cation-disordered rocksalt transition metal oxides and oxyfluorides for high energy lithium-ion cathodes". In: *Energy & Environmental Science* 13.2 (2020), pp. 345–373. ISSN: 1754-5692. DOI: 10.1039/C9EE02803J. URL: http://dx.doi.org/10.1039/C9EE02803J.

[12] Bin Ouyang et al. "Effect of Fluorination on Lithium Transport and Short-Range Order in Disordered-Rocksalt-Type Lithium-Ion Battery Cathodes". In: *Advanced Energy Materials* 10.10 (2020), pp. 1–11. ISSN: 16146840. DOI: 10.1002/aenm.201903240.

[13] Aziz Abdellahi et al. "Understanding the Effect of Cation Disorder on the Voltage Profile of Lithium Transition-Metal Oxides". In: *Chemistry of Materials* 28.15 (Aug. 2016), pp. 5373–5383. ISSN: 15205002. DOI: 10.1021/acs.chemmater.6b01438. URL: https://doi.org/10.1021/acs.chemmater.6b01438.

[14] Raphaële J Clément et al. "Short-Range Order and Unusual Modes of Nickel Redox in a Fluorine-Substituted Disordered Rocksalt Oxide Lithium-Ion Cathode". In: *Chemistry of Materials* 30.19 (Oct. 2018), pp. 6945–6956. ISSN: 0897-4756. DOI: 10.1021/acs.chemmater.8b03794. URL: https://doi.org/10.1021/acs.chemmater.8b03794.

[15] Eric J Wu, Patrick D Tepesch, and Gerbrand Ceder. "Size and charge effects on the structural stability of LiMO2 (M = transition metal) compounds". In: *Philosophical Magazine B* 77.4 (Apr. 1998), pp. 1039–1047. ISSN: 1364-2812. DOI: 10.1080/13642819808206403. URL: https://doi.org/10.1080/13642819808206403.

[16] John Reed and Gerbrand Ceder. "Role of Electronic Structure in the Susceptibility of Metastable Transition-Metal Oxide Structures to Transformation". In: *Chemical Reviews* 104.10 (Oct. 2004), pp. 4513–4534. ISSN: 0009-2665. DOI: 10.1021/cr020733x. URL: https://doi.org/10.1021/cr020733x.

[17] Jinhyuk Lee et al. "Reversible Mn2+/Mn4+ double redox in lithium-excess cathode materials". In: *Nature* 556.7700 (2018), pp. 185–190. ISSN: 1476-4687. DOI: 10.1038/s41586-018-0015-4. URL: https://doi.org/10.1038/s41586-018-0015-4.

[18] Yuan Yue et al. "Tailoring the Redox Reactions for High-Capacity Cycling of Cation-Disordered Rocksalt Cathodes". In: *Advanced Functional Materials* n/a.n/a (Jan. 2021), p. 2008696. ISSN: 1616-301X. DOI: https://doi.org/10.1002/adfm.202008696. URL: https://doi.org/10.1002/adfm.202008696.

[19] Zhengyan Lun et al. "Cation-disordered rocksalt-type high-entropy cathodes for Li-ion batteries". In: *Nature Materials* (2020). ISSN: 1476-4660. DOI: 10.1038/s41563-020-00816-0. URL: https://doi.org/10.1038/s41563-020-00816-0.

[20] William D Richards et al. "Fluorination of Lithium-Excess Transition Metal Oxide Cathode Materials". In: *Advanced Energy Materials* 8.5 (Feb. 2018), p. 1701533. ISSN: 1614-6832. DOI: 10.1002/aenm.201701533. URL: https://doi.org/10.1002/aenm.201701533.

[21] M Ménétrier et al. "NMR evidence of LiF coating rather than fluorine substitution in Li(Ni0.425Mn0.425Co0.15)O2". In: *Journal of Solid State Chemistry* 181.12 (2008), pp. 3303–3307. ISSN: 0022-4596. DOI: https://doi.org/10.1016/j.jssc.2008.09.002. URL: http://www.sciencedirect.com/science/article/pii/S0022459608004751.

[22] Zhengyan Lun et al. "Improved Cycling Performance of Li-Excess Cation-Disordered Cathode Materials upon Fluorine Substitution". In: *Advanced Energy Materials* 9.2 (Jan. 2019), p. 1802959. ISSN: 16146840. DOI: 10.1002/aenm.201802959. URL: https://doi.org/10.1002/aenm.201802959.

[23] Matthew J. Crafton et al. “Anion Reactivity in Cation-Disordered Rocksalt Cathode Materials: The Influence of Fluorine Substitution”. In: *Advanced Energy Materials* 10.35 (2020), pp. 1–12. ISSN: 16146840. DOI: 10.1002/aenm.202001500.

[24] Linze Li et al. “Fluorination-Enhanced Surface Stability of Cation-Disordered Rocksalt Cathodes for Li-Ion Batteries”. In: *Advanced Functional Materials* n/a.n/a (Apr. 2021), p. 2101888. ISSN: 1616-301X. DOI: https://doi.org/10.1002/adfm.202101888. URL: https://doi.org/10.1002/adfm.202101888.

[25] Robert A. House et al. “Lithium manganese oxyfluoride as a new cathode material exhibiting oxygen redox”. In: *Energy and Environmental Science* 11.4 (2018), pp. 926–932. ISSN: 17545706. DOI: 10.1039/c7ee03195e.

[26] Yuan Yue et al. “Redox Behaviors in a Li-Excess Cation-Disordered Mn–Nb–O–F Rocksalt Cathode”. In: *Chemistry of Materials* 32.11 (2020), pp. 4490–4498. ISSN: 0897-4756. DOI: 10.1021/acs.chemmater.9b05221.

[27] Dong Hwa Seo et al. “The structural and chemical origin of the oxygen redox activity in layered and cation-disordered Li-excess cathode materials”. In: *Nature Chemistry* 8.7 (2016), pp. 692–697. ISSN: 17554349. DOI: 10.1038/nchem.2524.

[28] Tzu-Yang Huang et al. “Deconvolution of intermixed redox processes in Ni-based cation-disordered Li-excess cathodes”. In: *Energy & Environmental Science* (2021). ISSN: 1754-5692. DOI: 10.1039/D0EE03526B. URL: http://dx.doi.org/10.1039/D0EE03526B.

[29] Zhengyan Lun et al. “Design Principles for High-Capacity Mn-Based Cation-Disordered Rocksalt Cathodes”. In: *Chem* 6.1 (2020), pp. 153–168. ISSN: 2451-9294. DOI: https://doi.org/10.1016/j.chempr.2019.10.001. URL: http://www.sciencedirect.com/science/article/pii/S2451929419304322.

[30] Christoph Bolli et al. “Operando Monitoring of F– Formation in Lithium Ion Batteries”. In: *Chemistry of Materials* 31.4 (Jan. 2019), pp. 1258–1267. DOI: 10.1021/acs.chemmater.8b03810.

[31] Young-Kyu Han, Jaeik Yoo, and Taeeun Yim. “Distinct Reaction Characteristics of Electrolyte Additives for High-Voltage Lithium-Ion Batteries: Tris(trimethylsilyl) Phosphite, Borate, and Phosphate”. In: *Electrochimica Acta* 215 (2016), pp. 455–465. ISSN: 0013-4686. DOI: https://doi.org/10.1016/j.electacta.2016.08.131. URL: https://www.sciencedirect.com/science/article/pii/S0013468616318667.

[32] Bryan D. Mccloskey et al. “Combining accurate O2 and Li2O2 assays to separate discharge and charge stability limitations in nonaqueous Li-O 2 Batteries”. In: *Journal of Physical Chemistry Letters* 4.17 (Aug. 2013), pp. 2989–2993. ISSN: 19487185. DOI: 10.1021/jz401659f.

[33] B. D. McCloskey et al. “Solvents’ Critical Role in Nonaqueous Lithium–Oxygen Battery Electrochemistry”. In: *The Journal of Physical Chemistry Letters* 2.10 (Apr. 2011), pp. 1161–1166. DOI: 10.1021/jz200352v.

[34] B. D. McCloskey et al. “Twin problems of interfacial carbonate formation in nonaqueous Li-O 2 batteries”. In: *Journal of Physical Chemistry Letters* 3.8 (2012), pp. 997–1001. ISSN: 19487185. DOI: 10.1021/jz300243r.

[35] Ivan Hung et al. “Isotropic High Field NMR Spectra of Li-Ion Battery Materials with Anisotropy ¿1 MHz”. In: *Journal of the American Chemical Society* 134.4 (Feb. 2012), pp. 1898–1901. ISSN: 0002-7863. DOI: 10.1021/ja209600m. URL: https://doi.org/10.1021/ja209600m.

[36] Z Gan and R R Ernst. “An Improved 2D Magic-Angle-Turning Pulse Sequence for the Measurement of Chemical-Shift Anisotropy.” eng. In: *Journal of magnetic resonance. Series A* 123.1 (Nov. 1996), pp. 140–143. ISSN: 1064-1858 (Print). DOI: 10.1006/jmra.1996.0227.

[37] Dominique Massiot et al. “Modelling one- and two-dimensional solid-state NMR spectra”. In: *Magnetic Resonance in Chemistry* 40.1 (Jan. 2002), pp. 70–76. ISSN: 0749-1581. DOI: https://doi.org/10.1002/mrc.984. URL: https://doi.org/10.1002/mrc.984.

[38] Sara E. Renfrew and Bryan D. McCloskey. “Quantification of Surface Oxygen Depletion and Solid Carbonate Evolution on the First Cycle of LiNi0.6Mn0.2Co0.2O2 Electrodes”. In: *ACS Applied Energy Materials* 2.5 (2019), pp. 3762–3772. ISSN: 25740962. DOI: 10.1021/acsaem.9b00459.

[39] Srinivasan Ramakrishnan et al. "Extended Interfacial Stability through Simple Acid Rinsing in a Li-Rich Oxide Cathode Material". In: *Journal of the American Chemical Society* 142.18 (Apr. 2020), pp. 8522–8531. ISSN: 15205126. DOI: 10.1021/jacs.0c02859.

[40] Daniil A Kitchaev et al. "Design principles for high transition metal capacity in disordered rocksalt Li-ion cathodes". In: *Energy & Environmental Science* 11.8 (2018), pp. 2159–2171. ISSN: 1754-5692. DOI: 10.1039/C8EE00816G. URL: http://dx.doi.org/10.1039/C8EE00816G.

[41] Jinhyuk Lee et al. "Determining the Criticality of Li-Excess for Disordered-Rocksalt Li-Ion Battery Cathodes". In: *Advanced Energy Materials* 11.24 (June 2021), p. 2100204. ISSN: 1614-6832. DOI: https://doi.org/10.1002/aenm.202100204. URL: https://doi.org/10.1002/aenm.202100204.

[42] Xuelong Wang et al. "The Role of Electron Localization in Covalency and Electrochemical Properties of Lithium-Ion Battery Cathode Materials". In: *Advanced Functional Materials* 31.2 (Jan. 2021), p. 2001633. ISSN: 1616-301X. DOI: https://doi.org/10.1002/adfm.202001633. URL: https://doi.org/10.1002/adfm.202001633.

[43] Sara E Renfrew and Bryan D McCloskey. "Residual Lithium Carbonate Predominantly Accounts for First Cycle CO2 and CO Outgassing of Li-Stoichiometric and Li-Rich Layered Transition-Metal Oxides". In: *Journal of the American Chemical Society* 139.49 (Dec. 2017), pp. 17853–17860. ISSN: 0002-7863. DOI: 10.1021/jacs.7b08461. URL: https://doi.org/10.1021/jacs.7b08461.

[44] Michael Metzger et al. "Origin of H2Evolution in LIBs: H2O Reduction vs. Electrolyte Oxidation". In: *Journal of The Electrochemical Society* 163.5 (2016), A798–A809. ISSN: 0013-4651. DOI: 10.1149/2.1151605jes. URL: http://dx.doi.org/10.1149/2.1151605jes.

[45] Yang Yu et al. "Coupled LiPF6 Decomposition and Carbonate Dehydrogenation Enhanced by Highly Covalent Metal Oxides in High-Energy Li-Ion Batteries". In: *Journal of Physical Chemistry C* 122.48 (Oct. 2018), pp. 27368–27382. ISSN: 19327455. DOI: 10.1021/acs.jpcc.8b07848.

[46] Anna T.S. Freiberg et al. "Li2CO3 decomposition in Li-ion batteries induced by the electrochemical oxidation of the electrolyte and of electrolyte impurities". In: *Electrochimica Acta* 346 (2020), p. 136271. ISSN: 00134686. DOI: 10.1016/j.electacta.2020.136271. URL: https://doi.org/10.1016/j.electacta.2020.136271.

[47] Yirui Zhang et al. "Revealing electrolyte oxidation via carbonate dehydrogenation on Ni-based oxides in Li-ion batteries by in situ Fourier transform infrared spectroscopy". In: *Energy & Environmental Science* 13.1 (2020), pp. 183–199. ISSN: 1754-5692. DOI: 10.1039/C9EE02543J. URL: http://dx.doi.org/10.1039/C9EE02543J.

[48] Jinhyuk Lee et al. "Mitigating oxygen loss to improve the cycling performance of high capacity cation-disordered cathode materials". In: *Nature Communications* 8.1 (2017), p. 981. ISSN: 20411723. DOI: 10.1038/s41467-017-01115-0. URL: https://doi.org/10.1038/s41467-017-01115-0.

[49] Chun Zhan et al. "Dissolution, migration, and deposition of transition metal ions in Li-ion batteries exemplified by Mn-based cathodes – a critical review". In: *Energy & Environmental Science* 11.2 (2018), pp. 243–257. ISSN: 1754-5692. DOI: 10.1039/C7EE03122J. URL: http://dx.doi.org/10.1039/C7EE03122J.

[50] Sophie Solchenbach et al. "Quantification of PF 5 and POF 3 from Side Reactions of LiPF 6 in Li-Ion Batteries". In: *Journal of The Electrochemical Society* 165.13 (2018), A3022–A3028. ISSN: 0013-4651. DOI: 10.1149/2.0481813jes.

[51] Bernardine L D Rinkel et al. "Electrolyte Oxidation Pathways in Lithium-Ion Batteries". In: *Journal of the American Chemical Society* 142.35 (Sept. 2020), pp. 15058–15074. ISSN: 0002-7863. DOI: 10.1021/jacs.0c06363. URL: https://doi.org/10.1021/jacs.0c06363.

[52] Aurélie Guéguen et al. "Elucidating the Reactivity of Tris(trimethylsilyl)phosphite and Tris(trimethylsilyl)phosphate Additives in Carbonate Electrolytes - A Comparative Online Electrochemical Mass Spectrometry Study". In: *ACS Applied Energy Materials* 3.1 (2020), pp. 290–299. ISSN: 25740962. DOI: 10.1021/acsaem.9b01551.

[53] Nan Xin et al. “Solubilities of six lithium salts in five non-aqueous solvents and in a few of their binary mixtures”. In: *Fluid Phase Equilibria* 461 (2018), pp. 1–7. ISSN: 0378-3812. DOI: https://doi.org/10.1016/j.fluid.2017.12.034. URL: https://www.sciencedirect.com/science/article/pii/S0378381217305186.

[54] Takayuki Aoshima et al. “Mechanisms of manganese spinels dissolution and capacity fade at high temperature”. In: *Journal of Power Sources* 97-98 (2001), pp. 377–380. ISSN: 0378-7753. DOI: https://doi.org/10.1016/S0378-7753(01)00551-1. URL: https://www.sciencedirect.com/science/article/pii/S0378775301005511.

[55] Dong H Jang and Seung M Oh. “Electrolyte Effects on Spinel Dissolution and Cathodic Capacity Losses in 4 V Li / Li x Mn2 O 4 Rechargeable Cells”. In: *Journal of The Electrochemical Society* 144.10 (1997), pp. 3342–3348. ISSN: 0013-4651. DOI: 10.1149/1.1838016. URL: http://dx.doi.org/10.1149/1.1838016.

[56] Dong H Jang, Young J Shin, and Seung M Oh. “Dissolution of Spinel Oxides and Capacity Losses in 4 V Li / Li x Mn2 O 4 Cells”. In: *Journal of The Electrochemical Society* 143.7 (1996), pp. 2204–2211. ISSN: 0013-4651. DOI: 10.1149/1.1836981. URL: http://dx.doi.org/10.1149/1.1836981.

[57] K. Edström, T. Gustafsson, and J. O. Thomas. “The cathode-electrolyte interface in the Li-ion battery”. In: *Electrochimica Acta* 50.2-3 SPEC. ISS. (2004), pp. 397–403. ISSN: 00134686. DOI: 10.1016/j.electacta.2004.03.049.

[58] Won Jong Lee et al. “Depth profile studies on nickel rich cathode material surfaces after cycling with an electrolyte containing vinylene carbonate at elevated temperature”. In: *Physical Chemistry Chemical Physics* 16.32 (2014), pp. 17062–17071. ISSN: 1463-9076. DOI: 10.1039/C4CP02075H. URL: http://dx.doi.org/10.1039/C4CP02075H.

[59] Ting Liu et al. “Surface phenomena of high energy Li(Ni1/3Co1/3Mn1/3)O2/graphite cells at high temperature and high cutoff voltages”. In: *Journal of Power Sources* 269 (2014), pp. 920–926. ISSN: 0378-7753. DOI: https://doi.org/10.1016/j.jpowsour.2014.07.051. URL: https://www.sciencedirect.com/science/article/pii/S0378775314010957.

[60] Judith Alvarado et al. “A carbonate-free, sulfone-based electrolyte for high-voltage Li-ion batteries”. In: *Materials Today* 21.4 (2018), pp. 341–353. ISSN: 1369-7021. DOI: https://doi.org/10.1016/j.mattod.2018.02.005. URL: http://www.sciencedirect.com/science/article/pii/S1369702118301731.

[61] Bharathy S Parimalam and Brett L Lucht. “Reduction Reactions of Electrolyte Salts for Lithium Ion Batteries: LiPF6, LiBF4, LiDFOB, LiBOB, and LiTFSI”. In: *Journal of The Electrochemical Society* 165.2 (2018), A251–A255. ISSN: 0013-4651. DOI: 10.1149/2.0901802jes. URL: http://dx.doi.org/10.1149/2.0901802jes.

[62] Peter Holstein, Robin K Harris, and Barry J Say. “Solid-state 19F NMR investigation of poly(vinylidene fluoride) with high-power proton decoupling”. In: *Solid State Nuclear Magnetic Resonance* 8.4 (1997), pp. 201–206. ISSN: 0926-2040. DOI: https://doi.org/10.1016/S0926-2040(97)00014-3. URL: https://www.sciencedirect.com/science/article/pii/S0926204097000143.